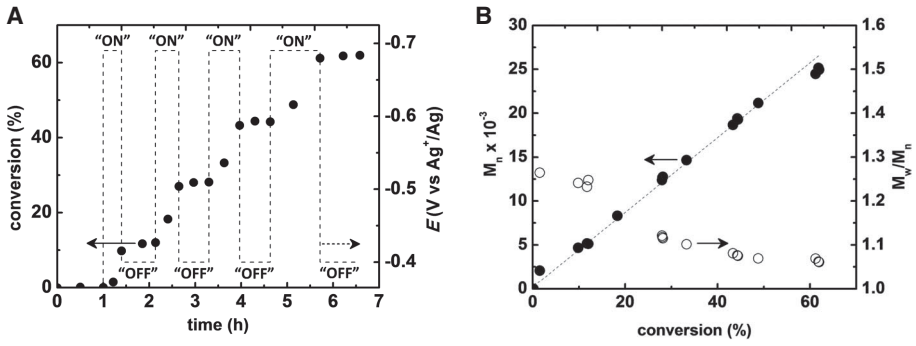

Fig. 4. (**A**) Conversion (solid circles) and applied potential (dashed line) with respect to time and (**B**) M_n and M_w/M_n with respect to conversion. Toggling between active and dormant states is represented by changes of the E_{app} values between −0.69V and −0.40 V versus Ag^+/Ag, respectively. Reaction conditions are identical to those stated in Fig. 2.

References and Notes

1. M. Szwarc, *Nature* **178**, 1168 (1956).
2. A. H. E. Müller, K. Matyjaszewski, *Controlled and Living Polymerizations: Methods and Materials* (Wiley-VCH, Weinheim, Germany, 2009).
3. K. Matyjaszewski, J. Xia, *Chem. Rev.* **101**, 2921 (2001).
4. M. Kamigaito, T. Ando, M. Sawamoto, *Chem. Rev.* **101**, 3689 (2001).
5. K. Matyjaszewski, T. P. Davis, *Handbook of Radical Polymerization*. (Wiley-Interscience, Hoboken, NJ, 2002).
6. T. E. Patten, J. Xia, T. Abernathy, K. Matyjaszewski, *Science* **272**, 866 (1996).
7. M. K. Georges, R. P. N. Veregin, P. M. Kazmaier, G. K. Hamer, *Macromolecules* **26**, 2987 (1993).
8. M. Kato, M. Kamigaito, M. Sawamoto, T. Higashimura, *Macromolecules* **28**, 1721 (1995).
9. J. Chiefari *et al.*, *Macromolecules* **31**, 5559 (1998).
10. J.-S. Wang, K. Matyjaszewski, *J. Am. Chem. Soc.* **117**, 5614 (1995).
11. L. H. Peeck, S. Leuthausser, H. Plenio, *Organometallics* **29**, 4339 (2010).
12. M. Benaglia *et al.*, *J. Am. Chem. Soc.* **131**, 6914 (2009).
13. H. J. Yoon, J. Kuwabara, J.-H. Kim, C. A. Mirkin, *Science* **330**, 66 (2010).
14. C. K. A. Gregson *et al.*, *J. Am. Chem. Soc.* **128**, 7410 (2006).
15. Y. Kwak, K. Matyjaszewski, *Macromolecules* **43**, 5180 (2010).
16. M. Tanabe *et al.*, *Nat. Mater.* **5**, 467 (2006).
17. J. Rzayev, J. Penelle, *Angew. Chem. Int. Ed.* **43**, 1691 (2004).
18. V. Bonometti, E. Labbé, O. Buriez, P. Mussini, C. Amatore, *J. Electroanal. Chem.* **633**, 99 (2009).
19. J. Qiu, K. Matyjaszewski, L. Thouin, C. Amatore, *Macromol. Chem. Phys.* **201**, 1625 (2000).
20. C. Y. Lin, M. L. Coote, A. Gennaro, K. Matyjaszewski, *J. Am. Chem. Soc.* **130**, 12762 (2008).
21. A. A. Isse *et al.*, *J. Am. Chem. Soc.*, ASAP (2011); doi: 10.1021/ja110538b.
22. W. A. Braunecker, K. Matyjaszewski, *Prog. Polym. Sci.* **32**, 93 (2007).
23. K. Min, H. Gao, K. Matyjaszewski, *J. Am. Chem. Soc.* **127**, 3825 (2005).
24. M. F. Cunningham, *Prog. Polym. Sci.* **33**, 365 (2008).
25. K. Min, K. Matyjaszewski, *Cent. Eur. J. Chem.* **7**, 657 (2009).
26. K. Matyjaszewski, N. V. Tsarevsky, *Nat. Chem.* **1**, 276 (2009).
27. K. Matyjaszewski *et al.*, *Proc. Natl. Acad. Sci. U.S.A.* **103**, 15309 (2006).
28. K. Matyjaszewski, H. Dong, W. Jakubowski, J. Pietrasik, A. Kusumo, *Langmuir* **23**, 4528 (2007).
29. W. Jakubowski, K. Matyjaszewski, *Angew. Chem.* **118**, 4594 (2006).
30. T. Pintauer, K. Matyjaszewski, *Chem. Soc. Rev.* **37**, 1087 (2008).
31. M. Nasser-Eddine, C. Delaite, P. Dumas, R. Vataj, A. Louati, *Macromol. Mater. Eng.* **289**, 204 (2004).
32. Materials and methods are available as supporting material on *Science* Online.
33. V. Hong, A. K. Udit, R. A. Evans, M. G. Finn, *ChemBioChem* **9**, 1481 (2008).
34. A. A. Isse, A. Gennaro, *J. Phys. Chem. A* **108**, 4180 (2004).

35. We acknowledge the U.S. National Science Foundation (grants DMR 09-69301 and CHE 10-26060) and the members of the CRP Consortium at Carnegie Mellon University for financial support. N.C.S. acknowledges the U.S. National Science Foundation for an American Competitiveness in Chemistry postdoctoral fellowship (CHE-1042006). A.J.D.M. and K.M. filed a U.S. provisional patent application (61/459,724) related to this work.

Supporting Online Material

www.sciencemag.org/cgi/content/full/332/6025/81/DC1
Materials and Methods
Figs. S1 to S5
References

30 December 2010; accepted 2 March 2011
10.1126/science.1202357

Thermochronometry Reveals Headward Propagation of Erosion in an Alpine Landscape

David L. Shuster,[1,2]*‡ Kurt M. Cuffey,[3,2]‡ Johnny W. Sanders,[2] Greg Balco[1]

Glacial erosion of mountain ranges produces spectacular alpine landscapes and, by linking climate with tectonics, influences a broad array of geophysical phenomena. Although the resultant landforms are easily identified, the timing and spatial pattern of topographic adjustment to Pleistocene glaciations remain poorly known. We investigated topographic evolution in the archetypal glacial landscape of Fiordland, New Zealand, using (U-Th)/He thermochronometry. We find that erosion during the past 2 million years removed the entire pre-Pleistocene landscape and fundamentally reshaped the topography. Erosion focused on steep valley segments and propagated from trunk valleys toward the heads of drainage basins, a behavior expected if subglacial erosion rate depends on ice sliding velocity. The Fiordland landscape illustrates complex effects of climate on Earth's surface morphology.

The characteristic landforms and large relief of many alpine landscapes indicate that the effect of glacial erosion over the past ~2.5 million years (My) has been profound (*1*, *2*). Understanding how this erosion progressed at the landscape scale over millions of years is essential for analyzing the connections between climate change, topography, and tectonic processes. Most quantitative studies of glacial landscape evolution rely on model simulations that calculate glacial erosion from poorly validated parameterizations [e.g., (*3*, *4*)]. Alternatively, direct observational constraints could reveal the evolution of topography and so guide model development [e.g., (*5*–*7*)]. Such constraints are difficult to obtain, however, because erosion itself effaces evidence of past topography.

We used the isotopic legacy of evolving crustal temperature conditions to constrain the history of relief development in a mountain landscape. We collected low-temperature thermochronometric measurements of 33 bedrock samples from along valley axes and up valley walls in high-relief drainage networks near Milford Sound in Fiordland, New Zealand (*8*). In this setting, patterns of topographic evolution over the past ~2 My are clearly decipherable because of a fortuitous correspondence between the temperature sensitivity of He isotopic techniques and the overall magnitude of Pleistocene exhumation. All samples were taken from a ~21-km–by–38-km region (Fig. 1). The valleys exhibit classic glacial forms, including U-shaped cross sections, concave longitudinal profiles dominated by low slopes, and deeply incised valley-head cirques with exception-

[1]Berkeley Geochronology Center, 2455 Ridge Road, Berkeley, CA 94709, USA. [2]Department of Earth and Planetary Science, University of California, Berkeley, CA 94720, USA. [3]Department of Geography, University of California, Berkeley, CA 94720, USA.

*To whom correspondence should be addressed. E-mail: dshuster@bgc.org
‡These authors contributed equally to this manuscript.

ally steep walls. The examined valleys are incised into strong plutonic rocks, primarily of the Arthur River and Darran complexes (*9*). Mean slopes of valley sides and cirque headwalls commonly exceed ~45° over horizontal and vertical scales of ~1.5 km. The dominant wavelength and relief of the regional surface topography are ~4 km and ~2 km, respectively (Fig. 1). This region currently receives abundant precipitation (>6 m/year) and lies along a tectonically active plate boundary. Oblique convergence of the Australian and Pacific plates, the source of mountain uplift, began about 6 My ago (*10*). Convergence has been accommodated primarily by deformation of weaker crust east of the Fiordland block.

Comparing measured apatite (U-Th)/He ages (*8*) to elevations for all sample sites reveals a broadly crescentic pattern (Fig. 2A); the youngest ages, ~1 My, generally occur at cirque floor elevations (~500 to 700 m), whereas older ages occur both at sea level (where ages approach ~2 My) and on summits (~2.5 My). This crescent-shaped age/elevation relationship appears in multiple valley systems, some of which drain NW from the main divide (to Milford Sound) and others to the SE (inland to Lake Te Anau). With one exception, all median (U-Th)/He ages are <2.5 My. Thus, these data primarily reflect processes active in the Pleistocene. The similarity between longitudinal age/elevation relationships of individual valleys (Fig. 2, B to D) and the regional age/elevation relationship (Fig. 2A) suggests both a consistent pattern of valley development across the region and an absence of localized tectonic influences on the age patterns (*8*).

We also analyzed samples using ^{4}He/^{3}He thermochronometry (*8*). Unlike (U-Th)/He ages, which are calculated from the total abundance of radiogenic ^{4}He relative to U and Th, the ^{4}He/^{3}He method constrains the spatial distribution of ^{4}He within an apatite crystal via controlled stepwise degassing of samples containing synthetic proton-induced ^{3}He (*11*). Such information delimits a sample's continuous cooling history through the temperature range ~80° to ~20°C (*12*). The cooling history, in turn, reveals aspects of topographic development not captured by the He ages alone.

Thermal histories derived from ^{4}He/^{3}He thermochronometry differ greatly across the landscape, even over small distances (Fig. 1). At the head of the North Branch Cleddeau valley, for example, rocks at the floor of an 1100-m-deep cirque cooled continuously over the past ~1 My, from temperatures of ~75° to 110°C to the present surface temperature (Fig. 1D). In contrast, rocks currently at the ridge crest resided at temperatures <25°C throughout this time interval. Superficially, these results suggest that much of the cirque relief developed over the past ~1 My. In this landscape of closely spaced valleys and high relief, however, the geothermal gradient depends strongly on position in the landscape; different thermal histories are expected at different sites, even if topography and mean exhumation rate were steady. To disentangle these factors, and to account for the effects of both surface erosion and rock uplift, we interpreted our data in the context of a three-dimensional thermokinematic finite-element model for subsurface temperature evolution (*13*).

This model allowed us to prescribe both the surface topography and the rock uplift as arbitrary functions of time and space. The sum of surface lowering and rock uplift then determined exhumation, the primary control on thermal histories. Uplift was assumed to be spatially uniform and steady, although we explored the effect of time-varying uplift rate in some sensitivity tests (*8*).

Using a variety of topographic histories, designed to represent idealized styles of morphological change, we calculated evolving temperatures over the past 4.0 My for the three regions delimited by white boxes in Fig. 1. Each calculation began at a steady state. We recorded the time series of temperatures along the particle paths leading to our sample sites on the modern surface. From such cooling histories, we calculated model (U-Th)/He ages and model ^{4}He/^{3}He release spectra as a function of sample characteristics (*14*); these results were compared to observations (*8*). We sought models that could simultaneously reproduce the key features of the data: the minimum of ages at cirque-floor elevations and the very steep age-elevation gradients on the sides of trunk valleys and at some valley heads.

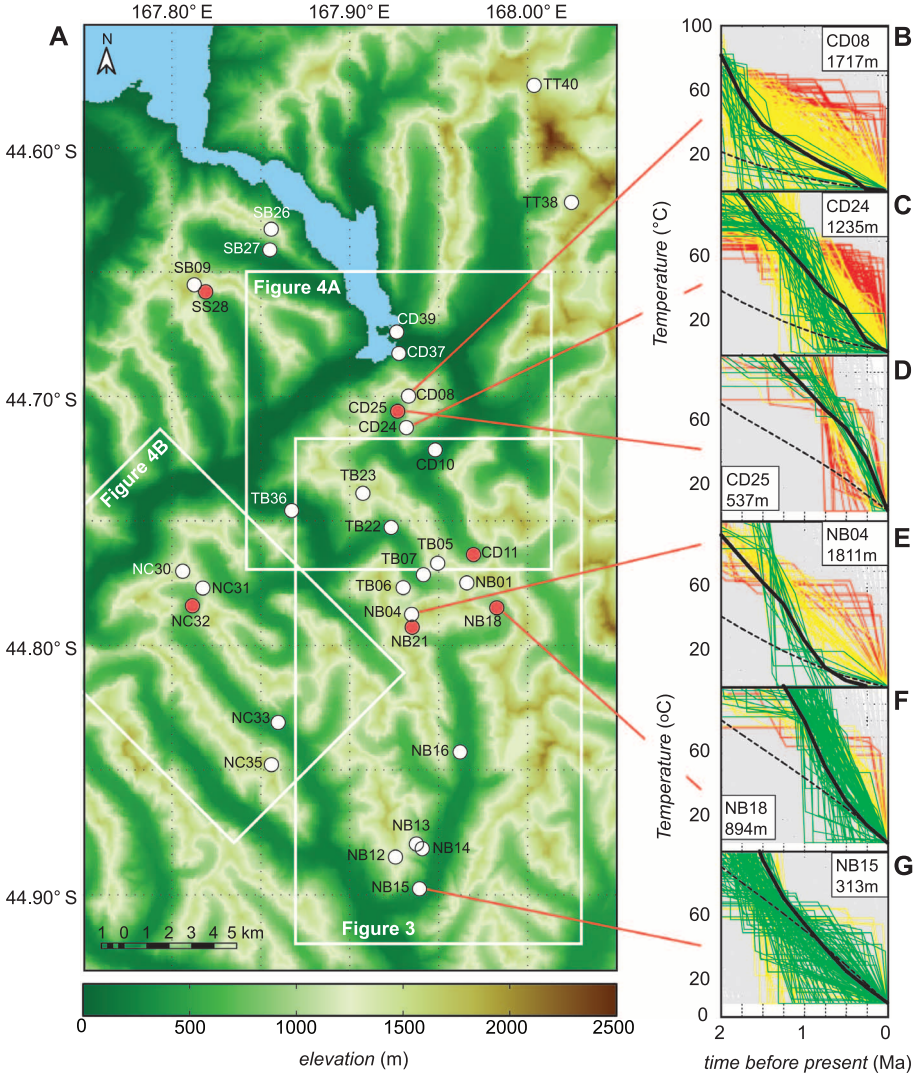

Fig. 1. Modern Fiordland topography and sample locations, together with cooling constraints from apatite ^{4}He/^{3}He thermochronometry. (**A**) Topography and bedrock sample locations; red denotes cirque-floor samples. White rectangles outline model domains (see Figs. 3 and 4). (**B** to **G**) Cooling paths from ^{4}He/^{3}He thermochronometry of select samples from the North Branch Cleddeau [(B) to (D)] and the Neale Burn drainages [(E) to (G)]. The colored sets of randomly generated cooling paths predict each observed (U-Th)/He age to within analytical uncertainty (±1σ); the gray paths do not. Yellow and red paths are progressively inconsistent, respectively, with the ^{4}He/^{3}He data (figs. S1 and S2), whereas green paths are most consistent (*12*). Cooling paths shown as solid black curves were predicted from the topographic evolution models shown in Figs. 3 and 4; the dashed black curves are predictions for steady-state topography, from models calibrated to match lowest-elevation samples (Fig. 2).

We attempted first to predict the observed (U-Th)/He ages by assuming steady topography and exhumation. These models predict a monotonic age/elevation relationship and can never reproduce the key features of the observations (Fig. 2). We then sought to fit the data with progressively more complex models (Fig. 2, E and F, and fig. S3). Rejected model classes include decreasing relief without changes of landform shape (i.e., exhumation proportional to present elevation); transition from an initially flat landscape to the present form (i.e., exhumation inversely related to present elevation); and deepening of valleys as their longitudinal profiles change from linear to concave.

The only class of models capable of matching the observations involves headward progression of erosion, so that deep exhumation of headwater regions (including cirques and drainage divides) occurred roughly 1 My after deep exhumation of the downstream segments of trunk valleys (Figs. 2 to 4). In the best-fitting models, prominent kilometer-scale topographic steps migrated upvalley (Figs. 3 and 4). Although idealized, this morphology resembles modern analogs in Norway and Antarctica, where steep valley ramps descend to level floors (*8*). Best-fitting models of this class imply basin-wide exhumation rates of 0.76 mm/year, partitioned between background exhumation and rock uplift of about 0.6 mm/year and maximum local bedrock lowering rates of ~4 mm/year (Fig. 3, D to F, and table S3). These models also succeed in predicting the local cooling paths constrained by $^{4}He/^{3}He$ data (Fig. 1, B to G).

In all cases, headward progression implies rapid erosion of steep valley segments as compared to adjacent flat segments downstream. Such behavior occurs in river systems, because boundary shear stress and the rate of energy expenditure increase with the slope (*15*). In Fiordland, however, the erosion pattern almost certainly arose from glacial action. Currently, glaciers survive on high slopes in this region of abundant snowfall. For most of the past 2 My, landscapes worldwide were considerably colder and icier than in the present interglacial period (*16*, *17*), and New Zealand glaciations generally followed world trends (*18*). In Fiordland, moreover, elevations upstream of the erosion fronts would have been substantially higher than at present (≥1.5 km according to our estimates; Figs. 3 and 4), placing a large portion of the drainage basins above the snow line even during interglacial periods. Furthermore, fluvial modification of glacial forms

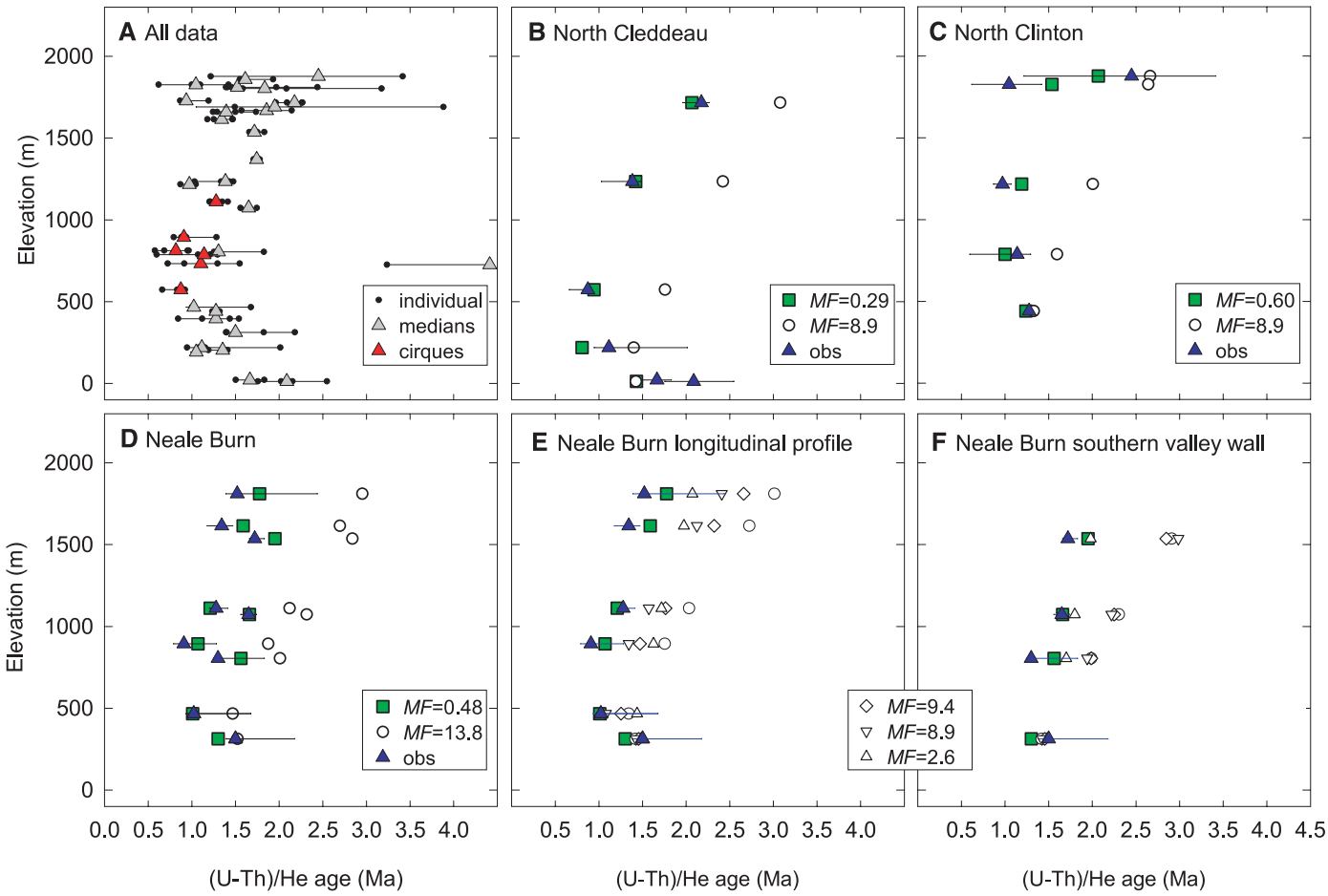

Fig. 2. Observed and modeled apatite (U-Th)/He ages and elevation relationships. (**A**) Observations for all Fiordland sample sites (Fig. 1). Both observations and modeled values are shown within (**B**) the North Branch Cleddeau, (**C**) the North Clinton, and (**D** to **F**) the Neale Burn drainages. Small black points are individual crystal ages; triangles and horizontal lines are the median age and range, respectively, observed for each sample. Squares are model ages predicted for the transient topographies illustrated in Figs. 3 and 4, calculated following (*13*) and (*14*), using each sample's crystal dimensions and U and Th concentrations. Open circles are model ages calculated instead with steady-state (modern) topography. By adjusting free parameters, steady-state models can match a subset of samples (the lowest-elevation ones in this case) but not all. Predicted ages from three alternative model classes are shown in (E) for samples along the axis of the Neale Burn drainage (NB15, NB16, NB18, NB21, NB04, and NB01), and (F) from its southern valley-wall transect (NB15, NB14, NB13, and NB12). To illustrate patterns, all models were calibrated to match the lowest-elevation sample; relative performance of the models is not sensitive to this choice (*8*). Open diamonds represent a proportional decrease in relief from 2.5 My ago to the present; fig. S3A shows the corresponding longitudinal profile evolution. The open downward triangles represent a continuous transition from a linear longitudinal profile (2.5 My ago) to the modern form; fig. S3B shows the profile evolution. The open upward triangles represent an extreme transition, between 1.75 and 0.75 My ago, from a 3-km plateau to the modern form; fig. S3C shows the profile evolution. MF is a misfit statistic calculated from the error-weighted differences between predicted and observed (U-Th)/He ages (*8*).

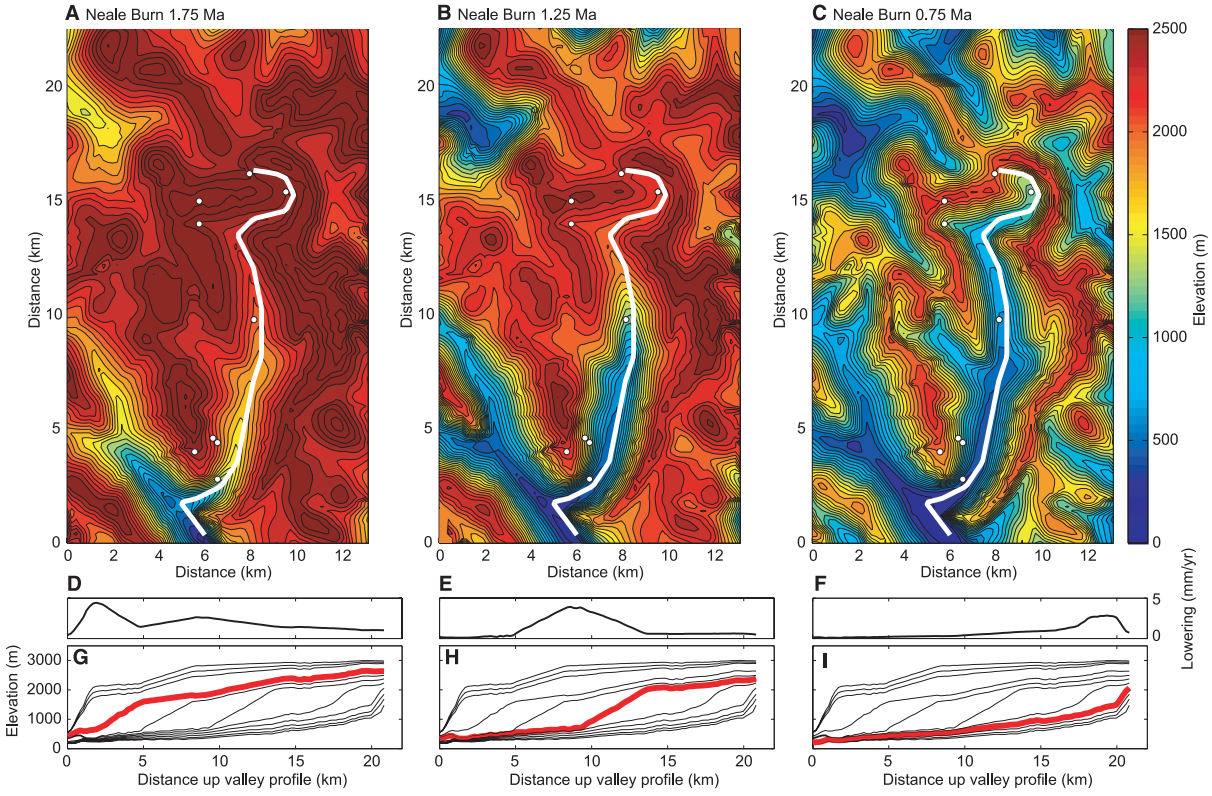

Fig. 3. Best-fit transient topographic scenario of headward erosion propagation along the Neale Burn drainage (domain outlined in Fig. 1). (**A** to **C**) The input topography at three representative model times (1.75, 1.25 and 0.75 My before the present, respectively). White points indicate sample locations, and white curves locate the longitudinal profiles shown in (**D** to **I**). (D) to (F) The local lowering rate (erosion rate minus uplift rate) along the profile, calculated for the preceding 250,000 years of each model time frame. (G) to (I) Model longitudinal profile evolution from 2.5 My ago to the present in 250,000-year intervals; red profiles correspond to time frames shown in (A) to (C). The high-elevation surfaces may represent the level of valley bottoms beneath a nearly isothermal relief.

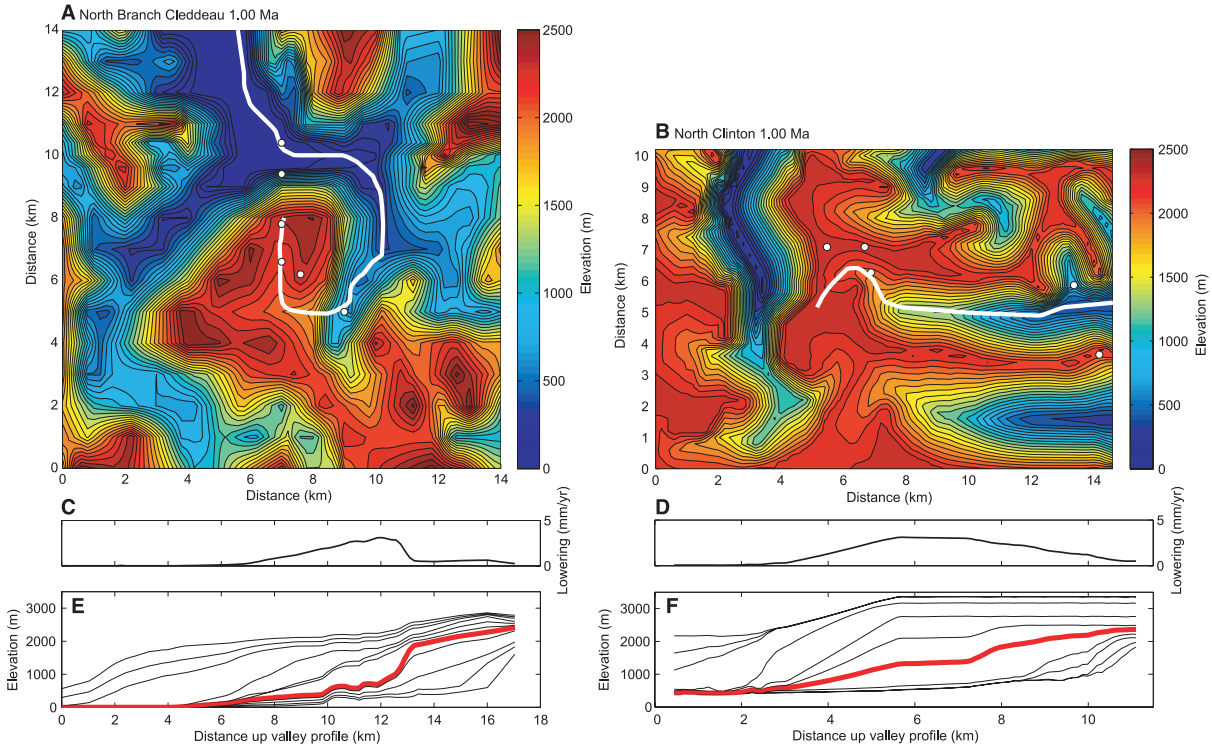

Fig. 4. Best-fit transient topographic scenarios of the North Branch Cleddeau and the North Clinton drainages. (**A** and **B**) The input topography shown at 1.00 My before the present for the model domains outlined in Fig. 1. As in Fig. 3, these models involve headward propagation of erosion along the longitudinal profile of each valley: the North Cleddeau (**C** and **E**) and the North Clinton (**D** and **F**). Panels and curve colors are as in Fig. 3.

during the Holocene has been minimal; features such as the abrupt step where the ~20-km^2 Bowen River basin joins Milford Sound indicate that rivers, even with large discharges and steep slopes, lack the capacity to incise the hard crystalline bedrock at high rates.

Glacial erosion by abrasion and quarrying occurs only if the ice slides along its bed. Theoretical treatments (*19*, *20*) indicate that erosion rate $\dot{e}$ increases with sliding velocity u_b; most simply, take $\dot{e} \propto u_b^r$, with r an unknown positive number. This suggests one origin for headward-propagating erosion in glacial valleys: Compared to more gently sloped sections upstream and downstream, a glacier flowing down a steep incline is thinner and faster, and hence more erosive. Simple calculations (*8*) imply that 10-fold contrasts in $\dot{e}$ along valley profiles (Figs. 3 and 4) most likely correspond to a parameter r value in the range ~1 to ~3. Others have proposed that feedbacks between quarrying, water pressure variability, and glacier geometry should cause up-valley propagation of subglacial bedrock steps with dimensions on the order of 10 to 100 m (*21*, *22*). The steep reaches associated with headward trending of erosion in Fiordland valleys are an order of magnitude larger. Valleys in our study region do display many steep bedrock facets with heights on the order of 100 m, but these features are too small to leave a record of propagation in the (U-Th)/He system.

Our thermochronometric data imply that large spatial variations of erosion rate determined the development of the Fiordland landscape. Our interpretation suggests that such variations arise from a glaciologically governed correlation between topography and sliding rate, together with a sliding-rate dependence of glacial erosion. A simple alternative approach to modeling glacial erosion—to use ice discharge as a proxy for erosion rate (*23*)—would not predict our observations because it precludes large contrasts of erosion rate over distances that are small compared to a glacier's length (except at special places such as tributary junctions).

Our results also suggest a landscape-scale target for model simulations. In Fiordland, the transition to Pleistocene climate initiated a massive reconfiguration of mountain range topography. Trunk valleys eroded rapidly at the outset, but their downstream portions have changed little in the past 1.5 My. By the mid-Pleistocene, erosion focused largely on drainage divides and valley heads, with decreasing area of high-elevation catchments. By 0.5 My ago, fundamental change had ceased, and average exhumation rates were the lowest in the Pleistocene. In essence, after the onset of glaciation, the mountain range was denuded from its flanks into its core and now changes only gradually. Thus, glaciation not only sculpted distinctive landforms but also systematically reshaped broad features of the range. Concerning debates about the response of mountain relief to glacial conditions (*24*), our study suggests that range-scale relief decreased during the Pleistocene, while local peak–to–valley floor relief increased transiently as erosion shifted headward.

References and Notes

1. A. Penck, *J. Geol.* **13**, 1 (1905).
2. D. E. Sugden, B. S. John, *Glaciers and Landscape* (Edward Arnold Publishers, London, 1976).
3. D. L. Egholm, S. B. Nielsen, V. K. Pedersen, J. E. Lesemann, *Nature* **460**, 884 (2009).
4. J. H. Tomkin, *Geomorphology* **103**, 180 (2009).
5. T. A. Ehlers, K. A. Farley, M. E. Rusmore, G. J. Woodsworth, *Geology* **34**, 765 (2006).
6. F. Herman, S. C. Cox, P. J. J. Kamp, *Tectonics* **28**, TC5011 (2009).
7. P. G. Valla, F. Herman, P. A. van der Beek, J. Braun, *Earth Planet. Sci. Lett.* **295**, 511 (2010).
8. Materials and methods are available as supporting material on *Science* Online.
9. A. L. Claypool *et al.*, *Tectonophysics* **359**, 329 (2002).
10. R. I. Walcott, *Rev. Geophys.* **36**, 1 (1998).
11. D. L. Shuster, K. A. Farley, J. M. Sisterson, D. S. Burnett, *Earth Planet. Sci. Lett.* **217**, 19 (2004).
12. T. F. Schildgen, G. Balco, D. L. Shuster, *Earth Planet. Sci. Lett.* **293**, 377 (2010).
13. J. Braun, *Comput. Geosci.* **29**, 787 (2003).
14. R. M. Flowers, R. A. Ketcham, D. L. Shuster, K. A. Farley, *Geochim. Cosmochim. Acta* **73**, 2347 (2009).
15. K. X. Whipple, *Annu. Rev. Earth Planet. Sci.* **32**, 151 (2004).
16. R. Bintanja, R. S. W. van de Wal, *Nature* **454**, 869 (2008).
17. S. C. Porter, *Quat. Res.* **32**, 245 (1989).
18. R. P. Suggate, *Quat. Sci. Rev.* **9**, 175 (1990).
19. B. Hallet, *Ann. Glaciol.* **2**, 23 (1981).
20. B. Hallet, *Ann. Glaciol.* **22**, 1 (1996).
21. R. B. Alley, *Geol. Soc. Am. Spec. Pap. 337* (1999), p. 1.
22. R. L. Hooke, *Geol. Soc. Am. Bull.* **103**, 1104 (1991).
23. R. S. Anderson, P. Molnar, M. A. Kessler, *J. Geophys. Res.* **111**, F01004 (2006).
24. K. X. Whipple, E. Kirby, S. H. Brocklehurst, *Nature* **401**, 39 (1999).

25. We thank Milford Helicopters, B. Lum, and the Caltech Noble Gas Lab for field and laboratory support; J. Braun and F. Herman for modeling guidance; and three anonymous referees for constructive comments. This work was supported by NSF grants EAR-0642869 (to D.L.S.) and EAR-0642830 (to K.M.C.) and by the Ann and Gordon Getty Foundation.

Supporting Online Material

www.sciencemag.org/cgi/content/full/332/6025/84/DC1
Materials and Methods
Figs. S1 to S7
Tables S1 to S3
References

28 September 2010; accepted 14 February 2011
10.1126/science.1198401

Microtomography of Partially Molten Rocks: Three-Dimensional Melt Distribution in Mantle Peridotite

Wenlu Zhu,[1]* Glenn A. Gaetani,[2] Florian Fusseis,[3] Laurent G. J. Montési,[1] Francesco De Carlo[4]

The permeability of the upper mantle controls melt segregation beneath spreading centers. Reconciling contradictory geochemical and geophysical observations at ocean ridges requires a better understanding of transport properties in partially molten rocks. Using x-ray synchrotron microtomography, we obtained three-dimensional data on melt distribution for mantle peridotite with various melt fractions. At melt fractions as low as 0.02, triple junctions along grain edges dominated the melt network; there was no evidence of an abrupt change in the fundamental character of melt extraction as melt fraction increased to 0.2. The porosity of the partially molten region beneath ocean ridges is therefore controlled by a balance between viscous compaction and melting rate, not by a change in melt topology.

The divergence of tectonic plates at oceanic spreading centers induces upwelling and melting of underlying mantle peridotite. The buoyant magmas rise through the mantle and are focused toward the ridge axis, forming new oceanic crust (*1*, *2*). Although up to 20% of the original peridotite may melt in this manner (*3*), melt extraction is efficient enough that only 1 to 3% porosity is observed in geophysical data sets (*4*, *5*). Broad regions of low seismic velocity detected under ridges imply that the mantle is relatively impermeable with a porosity of ~0.02 (*4*). However, geochemical data on mid-ocean ridge basalts (MORBs) indicate that once magma is formed, it segregates very efficiently from the residual peridotite (*6*, *7*). In particular, U-series disequilibria in MORB (*8*–*11*) imply a well-connected permeable mantle that allows efficient extraction of melt fractions lower than 0.01.

Although thermodynamic models of textural equilibrium predict that melt resides in channels along grain edges (i.e., triple junctions) (*12*, *13*), observations of synthetic olivine-basalt aggregates suggest that melt is present both in grain edge channels and as grain boundary films (*14*, *15*). If grain edge melt channels are few at melt fractions $\phi < 0.02$ and they are connected via grain boundary melt films (*15*), the less permeable films may limit the overall permeability at low porosity (*14*). At $\phi > 0.02$, channels become directly interconnected and permeability increases by several orders of magnitude (*14*). However, this model is based on two-dimensional

[1]Department of Geology, University of Maryland, College Park, MD 20742, USA. [2]Department of Geology and Geophysics, Woods Hole Oceanographic Institution, Woods Hole, MA 02543, USA. [3]Western Australian Geothermal Centre of Excellence, The University of Western Australia, Crawley, Australia. [4]Advanced Photon Source, Argonne National Laboratory, Argonne, 60439, USA.

*To whom correspondence should be addressed. E-mail: wzhu@umd.edu

Supporting Online Material for

Thermochronometry Reveals Headward Propagation of Erosion in an Alpine Landscape

David L. Shuster,* Kurt M. Cuffey, Johnny W. Sanders, Greg Balco

*To whom correspondence should be addressed. E-mail: dshuster@bgc.org

Published 1 April 2011, *Science* **332**, 84 (2011)
DOI: 10.1126/science.1198401

This PDF file includes:

Materials and Methods

Apatite (U-Th)/He dating

(U-Th-Sm)/He ages of individual apatite crystals were measured according to standard procedures (*S1*) at the Caltech Noble Gas Laboratory and, at the Berkeley Geochronology Center, from the $^4He/^3He$ analyses (see below). All individual (U-Th)/He ages, crystal characteristics and sample locations appear in Table S1.

$^4He/^3He$ thermochronometry

In apatite $^4He/^3He$ thermochronometry, the naturally occurring spatial distribution of radiogenic ^4He is constrained by controlled, sequential degassing analysis of crystals containing a spatially uniform, proton-induced distribution of ^3He (*S2*-*S5*). Milligram quantities of apatite crystals were separated from bedrock (collected at locations shown in Fig. 1) and loaded into Sn foil within Teflon containers. All samples were axially aligned within a glass confinement tube and simultaneously exposed to a proton beam (*S3, S4*) with incident energy ~220 MeV over a continuous 8 hour period at The Francis H. Burr Proton Therapy Center; the total proton fluence was $\sim 4.6 \times 10^{15}/cm^2$.

From each irradiated aliquot, individual crystals were selected for euhedral shape, uniform size, and absence of visible mineral inclusions; the crystals were photographed and dimensions measured (*S6*) using a calibrated binocular microscope. Single crystals were then loaded within PtIr packets and sequentially heated in multiple steps under ultra-high vacuum using a feedback-controlled 70 W laser diode at the Berkeley Geochronology Center Noble Gas Thermochronometry Lab. The extraction temperature was measured and controlled using a calibrated optical pyrometer system. The molar ^3He abundance and the $^4He/^3He$ ratio were measured after each heating step using calibrated pulse-counting sector-field mass spectrometry. The heating schedules were optimized to uniformly distribute $^4He/^3He$ measurements as a function of ΣF^3He, and not to quantify He diffusion kinetics in apatite. Corrections were made for blank contribution to ^3He and ^4He measurements (measured from room-temperature "extractions" interspersed every 6 steps throughout the analysis); correction uncertainty was propagated into ratio uncertainties reported ($\pm 1\sigma$ standard deviation) in Table S2.

Following the stepped heating analysis, U, Th and Sm molar abundances were measured by isotope dilution using standard ICP-MS procedures at Caltech. A (U-Th)/He age was then calculated from the ratio of these abundances to the sum of ^4He measured via incremental heating and by correcting for the proportion of α particles retained within each crystal (*S6*). Due to the young (U-Th)/He ages generally observed in this region, our application of $^4He/^3He$ thermochronometry was ultimately limited by the ^4He abundance within individual crystals. Many analyzed samples produced $^4He/^3He$ release spectra which did not provide additional thermal constraint beyond the (U-Th)/He age alone (i.e., the individual $^4He/^3He$ step uncertainties were large, primarily due to ^4He blank corrections), which appear in Table S1. For example, by comparing results shown in Fig. S2C and Fig. S1C, it is readily apparent that as the uncertainty in measured $^4He/^3He$ ratios increases, the permissible cooling paths converge on those which are constrained solely from the (U-Th)/He age (i.e., all colored paths).

Assumptions

In our interpretation of (U-Th)/He ages and $^4He/^3He$ release spectra, we assume that U and Th are uniformly distributed within individual apatite crystals and that the ^4He diffusion kinetics of each sample is influenced by observed U and Th concentrations (*S7*). We also assume that the ages primarily record bedrock cooling due to exhumation and evolution of surface topography. If local cooling effects due to groundwater fluxes were sufficiently large, they could potentially increase ages locally, for example in valley bottoms. However, we observe both the youngest and some of the oldest ages in such locations. Likewise, rearrangement by faulting, or transport along local fractures, would disrupt the systematic patterns observed in Fig. 2. However, such effects, or other unidentified complications, may account for the apparently anomalous ages, ~4 Ma, at site TB07.

Modeling strategy

We specify the history of topography and apply it as a boundary condition on a thermal model. Together with a specified uplift rate (assumed spatially uniform), the topographic history determines erosion rates as a function of space and time (erosion rate = uplift rate + rate of surface lowering). The thermal model predicts time-temperature histories for our samples, which in turn imply predicted (U-Th)/He ages and ^4He distributions. The problem is to choose the topographic evolution that best predicts the observed ages and $^4He/^3He$ results.

This problem is potentially vastly over-parameterized, given that an infinite number of topographic scenarios can be envisioned. Because of this, our modeling approach is to consider several different classes of idealized transient topographic scenarios. The classes are: (1) topographic steady-state; (2) decrease in relief without changes of landform shape (i.e., exhumation proportional to present elevation); (3) transition from an initially flat landscape to the present form (i.e., exhumation inversely related to present elevation); (4) deepening of valleys as their longitudinal profiles change from linear to concave; and (5) headward propagation of steep valley segments through the drainage network. We then determined whether each of these classes could predict the entire set of observations.

In all cases, the topographic changes were introduced as perturbations of the modern elevations, so that the planform configuration of drainages did not change. Each topographic scenario consists of a sequence of 11 frames depicting the elevations at successive times (the final frame being the modern topography). Scenarios were constructed by first defining the sequence of longitudinal profiles and widths for the valley bottoms. Elevations of ridge-lines and summits in the intervening uplands were calculated as a linear function of modern topography, with a uniform offset from sea-level and a proportional scaling of relief. The rest of the elevation model was then calculated by interpolation. Conclusions reported here about patterns of erosion are not sensitive to the values used for offset and scaling of the upland summits, because temperature gradients within narrow peaks and ridges are small; it is the timing and

pattern of valley incision that governs spatial variations of cooling histories in this landscape.

The idealized classes of landform evolution tested here are all plausible in light of basic geomorphic principles. From such principles we expect erosion rates in a homogeneous rock mass to vary systematically as a function of position in the drainage network and as a function of topographical variables such as slope. The importance of our strategy is that it allowed us to (i) limit the number of free parameters, and (ii) avoid making assumptions about erosional processes and how they varied in time and space. We specifically wished to interpret our data without recourse to a landscape evolution model that relies on parameterizations for erosion and transport processes. All such models embody a large number of poorly constrained but interacting assumptions. They should not necessarily be used to regulate the reconstruction of topographic histories from independent data.

Model parameters

In addition to the evolving surface topography, free parameters in the model were the rock uplift rate, the effective crustal thermal diffusivity, and two variables that effectively determine the background geothermal gradient: the rate of crustal heat production and the temperature at the base of the model domain (Table S3). Node spacing was selected so that calculated temperatures matched the high-resolution limit to within 1 ^{o}C. Thermal parameters were selected so that the background geothermal gradient in the upper crust was in the range 20-45 ^{o}C/km (*S8*). Best-fitting model results used the high end of this range; a high gradient minimizes the magnitude of differential exhumation needed to match patterns in the data. Thus, excepting sensitivity tests, we used the same thermal parameters for all domains and topographic scenarios, and optimized models by adjusting only the uplift rate.

Misfit Statistic (*MF*)

To quantify the performance of each model of evolving surface topography in predicting the observed (U-Th)/He ages within a given drainage basin, we use an error weighted misfit statistic (*MF*),

$$MF = \frac{1}{n}\sum_{i=1}^{n}\left(\frac{A_{p,i} - A_{m,i}}{\sigma_p + \sigma_{m,i}}\right)^2 ,$$

where n is the number of ages measured within the valley, A_m and A_p are the measured (median) and predicted He ages, respectively, σ_m is the measurement uncertainty (1 standard deviation in each sample's age population), and σ_p is the model imprecision (σ_p = 0.1 Ma).

Sensitivity and Robustness

We conducted a wide array of sensitivity studies to establish that none of the model results or conclusions regarding topographic development presented herein is qualitatively affected by our choices for model parameter values. For this study region, the large amplitude of the dominant topography relative to its wavelength significantly disconnects the pattern of subsurface isotherms from the pattern of ridges and valleys; the closure temperature isotherms for the systems considered here (between ~50-100 ^{o}C) are not significantly perturbed by the current topography. Thus spatial patterns in predicted quantities depend only weakly on thermal parameters such as effective diffusivity, and depend most strongly on local rock exhumation related to changing topography. Our results, however, have one unavoidable quantitative ambiguity; because the relief scenarios are constrained by cooling ages, there is a direct trade-off between the nominal geothermal gradient and the mean magnitude of inferred exhumation (and hence rock uplift). We have no good independent constraint on the local geothermal gradient; if our value is too large by a factor of, say, 1.5, then our inferred mean exhumation is too small by a factor of about 2/3.

Figure S4A-B illustrates, using a steady-state topography for clarity, the effect on predicted ages of changing the uplift rate but without changing values for thermal parameters. Figure S4C-D does the same, but for varying thermal parameters at a constant uplift rate. These sorts of sensitivities have been well elaborated in the thermochronologic literature [e.g., (*S9-S11*)].

Concerning the evaluation of different classes of topographic development, we found that unsuccessful models produced not only poor values for fit statistics but also systematic elevation-dependent residuals with respect to the (U-Th)/He ages. This clearly excludes them as plausible scenarios. The headward propagation model, in contrast, produced good fits and did not produce systematic residuals. In fact, this is the only class of models that produces the middle-elevation minimum in (U-Th)/He ages that is the most obvious feature of the data set, while simultaneously predicting the very steep age-elevation gradients on the sides of trunk valleys and at some valley heads.

Our confidence in the validity of our general conclusions arises from the ability of some model scenarios but not others to match *simultaneously* the following key specific features of the data:

(1) minimum ages at cirque-floors
(2) downstream valley-bottom ages of greater than 1.2 Ma in all three drainage basins
(3) negligible age differences between drainage divide summits and downstream valley bottoms in the Neale Burn and North Clinton Basins
(4) a small age difference between the summit at the head of the Cleddeau and the deep trunk valley (Milford Sound) adjacent to it
(5) the young age (~1 Ma) of the drainage divide at the head of the North Clinton, despite its location adjacent to the deep valley of the Arthur River to the west
(6) the steep age-elevation gradient on the southern valley wall at the downstream end of the Neale Burn (Fig. 2F)
(7) the time-dependence of cooling histories as shown in Figure 1 of the manuscript

We emphasize that the ages and cooling histories of each sample can only be interpreted in the context of a numerical model, because of strong effects of high-relief, narrow-wavelength topography on thermal gradients. A rock exposed at the summit of a mountain, for example, experiences very different cooling histories – even for the same exhumation history – if the mountain sits adjacent to a deep valley than if it is a broad dome on a plateau. For the same reason, model results for different sample sites are in some cases interdependent in complex ways. This increases the robustness of our interpretations.

One issue concerning the robustness of our conclusions concerns the distinction between erosion and topography. Our results are firmest with respect to the former. To explain our data, it is essential that over the Pleistocene the focus of erosion shifted toward the headwaters of drainage basins. The correspondence between such a shift and the development of topography is less clear because of the role of uplift and the limitations of our data set, but we can still reach strong conclusions. To illustrate, consider an alternative topographic history for the Neale Burn drainage, as in Figure S5A. In this case, headward trending of erosion occurs independent of up-valley propagation of topographic forms; instead, it arises from an ad-hoc change in the relationship between erosion rate and geomorphic variables (position along the drainage, and slope). This alternative scenario predicts a crescent-shaped distribution of ages with elevation, as Figure S5C demonstrates for different values of uplift rate (see Figure S5B for uplift rates). At all uplift rates, however, it predicts too large an age difference between the downstream valley bottom and the drainage divides (Fig. S5C) and too large an age-elevation gradient (dAge/dz) on the downstream, southern valley wall (Fig. S5D). To resolve this problem, in turn, we can suppose that the background uplift and exhumation rate decreased through the first part of the Pleistocene, as shown in Fig. S5B (triangle symbols). A factor-of-three decrease is insufficient to correct the problem (Fig S5F). A factor-of-five decrease comes close to matching the gradient but simultaneously underpredicts ages of the two low-elevation (trunk valley) samples (Fig. S5E). We conclude that it is difficult but not impossible to match the data with a topographic scenario such as Fig. S5A. Doing so requires several dubious assumptions: (1) a fundamental change in the relationship between erosion and geomorphological variables, (2) an unusual initial longitudinal profile and its persistence for >1 Ma, and (3) large temporal variations in uplift rate. We reject this alternative as implausible but recognize that the idealized topographic development accepted as our best-fit model and shown in Figure 3 (main text) is undoubtedly too simple.

Simple Analysis of Erosion Rate Contrasts

The following idealization pertains to a typical temperate valley glacier; that is, one with a basal drag of about 10^5 Pa, a driving stress of 1 to 2 × 10^5 Pa, and flow by a combination of sliding and internal deformation [(*S12*); pp. 295-302].

Consider a glacier flowing down a long and steep ramp in its longitudinal profile and then onto a flat. We will denote variables at a location on the ramp with the subscript 1, and those on the flat below with a subscript o. Let α indicate ice surface slope, β bed slope, H ice thickness, u_b basal (sliding) velocity, u_d the depth-mean deformational velocity, and u the total depth-mean velocity.

- Geometrical approximations

- The steep section can be regarded as a slab, hence $\alpha_1 = \beta_1$ [(*S12*); p.298].

- In the flat section, $\beta_o = 0$, but α_o must be roughly

$$\alpha_o = \frac{\tau_o}{f_o \rho g H_o} \approx \frac{c}{f_o H_o} \qquad (1)$$

  according to the plasticity approximation for ice [(*S12*); p.298]. Here τ_o and ρ denote the yield stress and density for ice, f_o denotes the shape factor accounting for drag by valley walls, and $g = 9.8$ ms^{-2}. The constant c has a value of about 11 m.

- The valley width is assumed uniform.

- Approximation of flux equivalence

The transition between the steep and flat sections occurs over a distance small compared to the entire glacier length. Thus the ice flux can be approximated as uniform. Consequently, given a uniform valley width,

$$u_1 H_1 = u_o H_o \qquad (2)$$

The argument developed here does not apply to situations with spatially varying fluxes, such as confluences of tributaries with trunk glaciers, or variations along a large fraction of the glacier's length.

- Definition of sliding fraction

Define the variable ξ as the fraction of mean velocity due to sliding: hence $u_b = \xi u$. Then

$$u = \frac{u_d}{1-\xi} \ . \tag{3}$$

- Contrast of erosion rates

The rate of erosion ($\dot{e}$) depends on a power r of the sliding velocity: $\dot{e} \propto u_b^r$. Thus the amplification of erosion rate in the steep section relative to the flat section is

$$\frac{\dot{e}_1}{\dot{e}_o} = \left[\frac{u_{b1}}{u_{bo}}\right]^r = \left[\frac{\xi_1 H_o}{\xi_o H_1}\right]^r , \tag{4}$$

in which the second equality follows from Eq. 2 and the definition of ξ.

- Contrast of ice thicknesses

The immediate goal is to replace the ratio of thicknesses in Eq. 4 with a ratio of slopes, because β_1 is a known feature of the landscape. The substitution could be made by using the plasticity approximation, but a more accurate approach is to apply the relation for the deformational component of velocity or flux [(*S12*); pp.309-310]. Together with Eq. 3

$$\text{flux} = K \frac{f^n}{1-\xi} H^{n+2} \alpha^n \tag{5}$$

where K represents a constant for temperate ice, f an order-one parameter accounting for drag by valley walls, and n the creep exponent for ice.

- Contrast of erosion rates: continued

Using Eq. 5 to write H in terms of α, substituting into Eq. 4, and setting $\alpha_1 = \beta$ gives an erosion rate ratio of:

$$\frac{\dot{e}_1}{\dot{e}_o} = \left[\frac{\xi_1}{\xi_o}\left[\frac{1-\xi_o}{1-\xi_1}\right]^{1/[n+2]}\left[\frac{f_1\beta}{f_o\alpha_o}\right]^{n/[n+2]}\right]^r . \tag{6}$$

Because $n \approx 3$, the exponents involving n are about 0.2 and 0.6, respectively.

To proceed requires either making a substitution for α_o or specifying its value. Because ice thickness is easiest to think about geomorphologically, we use the plasticity approximation (Eq. 1) to replace α_o with H_o. An alternative that would allow use of the more accurate Eq. 5 is to write α_o in terms of flux. However, α, H, and flux all vary significantly over time as the glacier waxes and wanes. In this context, the plasticity approximation (which for typical alpine glaciers usually gives ice thicknesses to an accuracy of order 10%) is sufficient.

The final relation is

$$\frac{\dot{e}_1}{\dot{e}_o} = \left[\frac{\xi_1}{\xi_o} \left[\frac{1-\xi_o}{1-\xi_1} \right]^{1/[n+2]} \left[\frac{f_1}{c} H_o \beta \right]^{n/[n+2]} \right]^r . \qquad (7)$$

If the exponent r is omitted, the whole term equals the contrast in basal sliding velocities, u_{b1}/u_{bo}.

- Application of the theory

To use Eq. 7 it is necessary to specify values for sliding fraction (ξ) at both sites, drag factor (f_1) and bed slope (β) on the steep ramp, and ice thickness on the flat below (H_o). For narrow valleys, as in Fiordland, $f \approx 0.5$ (*S13*). Observed sliding fractions (ξ) of bedrock-floored temperate mountain glaciers cover the whole range from near zero to near unity [(*S12*); p.228], but it is unusual to not have a significant component of both deformation and sliding; a range of ξ from 0.2 to 0.8 covers most cases.

Our topographic reconstructions shown in Figures 3 and 4 suggest rather steep ramp slopes ($\beta \approx 0.2$) but cannot constrain them narrowly. The range 0.1 to 0.3 seems most likely (the lower bound constrained by our reconstructions, the upper bound by plausibility). Ice thicknesses H_o must have varied over time, from zero to greater than 1 km. We will use values of 500 m and 1000 m as representative of active ice in these deep valleys.

Finally, our reconstructions (Fig. 3D-F and Fig. 4C-D) require that, as an order of magnitude,

$$\frac{\dot{e}_1}{\dot{e}_o} \sim 10 . \qquad (8)$$

Taking this value as given, the implied erosion rate exponent r can be determined from the logarithm of Eq. 7.

- Results for the case of uniform sliding fraction

Choosing $\xi_o = \xi_1 = 0.5$ gives the following results. The corresponding ratios of sliding rates range from 1.64 to 4.80.

Inferred values of r			
		β	
	0.1	0.2	0.3
H_o = 500 m	4.7	2.5	2.0
H_o = 1000 m	2.5	1.7	1.5

- Results for a case of non-uniform sliding fraction

Sliding fraction is likely to be greater in the steep section than on the flat section [(*S14*); p. 62]. Using $\xi_o = 0.2$ and $\xi_1 = 0.8$, a rather large contrast, gives the following results. The corresponding ratios of sliding rates range from 8.6 to 25.

Inferred values of r			
		β	
	0.1	0.2	0.3
H_o = 500 m	2.5	2.1	0.81
H_o = 1000 m	2.1	0.77	0.71

Apparent erosion rates

We infer mean erosion rates of about 0.6 mm/yr, with local values as high as 4 mm/yr. Given that the geothermal gradient is not known from measurements, these values may deviate from the true ones by a factor of a few. Regardless, they are plausible values in that they fall within the range of inferred modern basin-wide glacier erosion rates from other mountain ranges. Erosion rates of order 1 mm/yr are typical for Scandinavia, the European Alps, Alaska, Iceland, and Asia [(*S12*), p. 278]. The highest estimates of long-term rates are about 15 mm/yr, from Southeast Alaska. We would be surprised if the crystalline rocks of Fiordland eroded so rapidly.

Modern Topographic Analogs

The inferred mid-Pleistocene topographies of best-fitting models shown in Figs. 3-4 resemble several modern analogs at high latitudes. Examples include incised valleys in the Jostedalsbreen (glacier) region of Norway (Fig. S6) and in the Boydell Glacier and Drygalski Glacier regions of the northern Antarctic Peninsula (Fig. S7). In each of these locations, ice originating on a highland flows down steep topographic steps and onto flat-floored valleys. In cases shown in Figs. S5 the steps are ~1.2 km in the vertical dimension with average longitudinal slopes of 0.2 to 0.4. They occur along longitudinal profiles at transitions between broad highlands and deeply incised valleys.

Figure S1

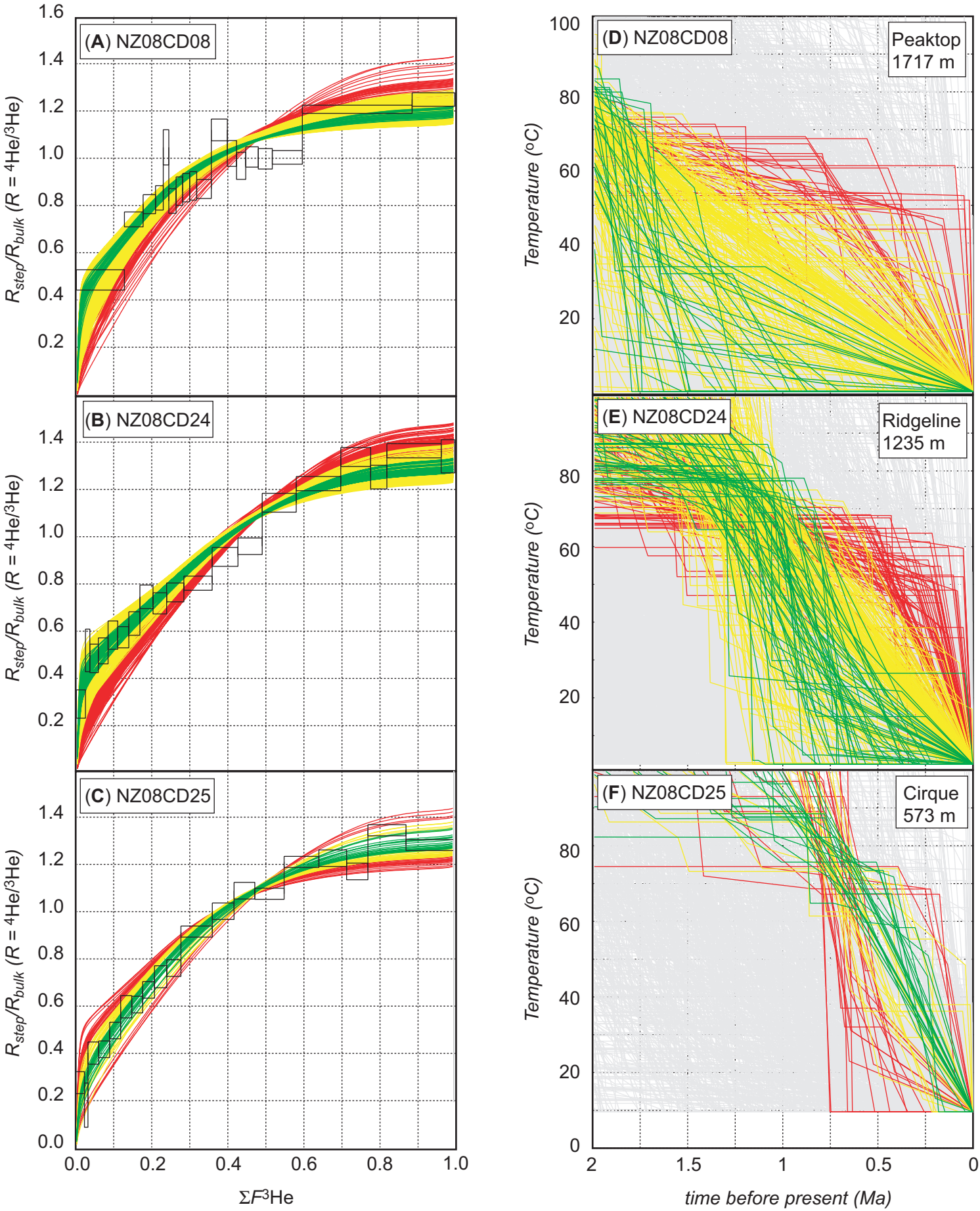
(A) NZ08CD08
(B) NZ08CD24
(C) NZ08CD25
(D) NZ08CD08
Peaktop
1717 m
(E) NZ08CD24
Ridgeline
1235 m
(F) NZ08CD25
Cirque
573 m
R_{step}/R_{bulk} ($R = {}^4He/{}^3He$)
ΣF^3He
Temperature (°C)
time before present (Ma)

Fig. S1. $^4He/^3He$ thermochronometry results for samples from the North Cleddeau valley shown in Fig. 1. Observed $^4He/^3He$ ratio evolution diagrams (**A-C**) and model cooling paths (**D-E**) for NZ08-CD08 (1717 m), NZ08-CD24 (1235 m) and NZ08-CD25 (573 m), respectively. The measured $^4He/^3He$ ratio of each degassing step (R_{step}) is normalized to the bulk ratio (R_{bulk}) and plotted versus the cumulative ^3He release fraction ($\sum F^3He$) (*S2, S3*). Open black boxes indicate 1 standard error (vertical) and integration steps (horizontal) (see Materials and Methods above and Table S2). Colored lines show the predicted $^4He/^3He$ ratio evolution diagrams **(A-C)** for randomly generated cooling paths **(D-F),** each of which predicts the observed (U-Th-Sm)/He age of each sample to within analytical uncertainty (±1σ standard deviation). They gray cooling paths shown in (**D-F**) fail to predict the observed (U-Th)/He age. Cooling paths shown in yellow and red are progressively inconsistent, respectively, with the $^4He/^3He$ data, whereas green paths are most consistent (*S5*) and are equivalent to those shown in **Fig. 1B-D**.

Figure S2

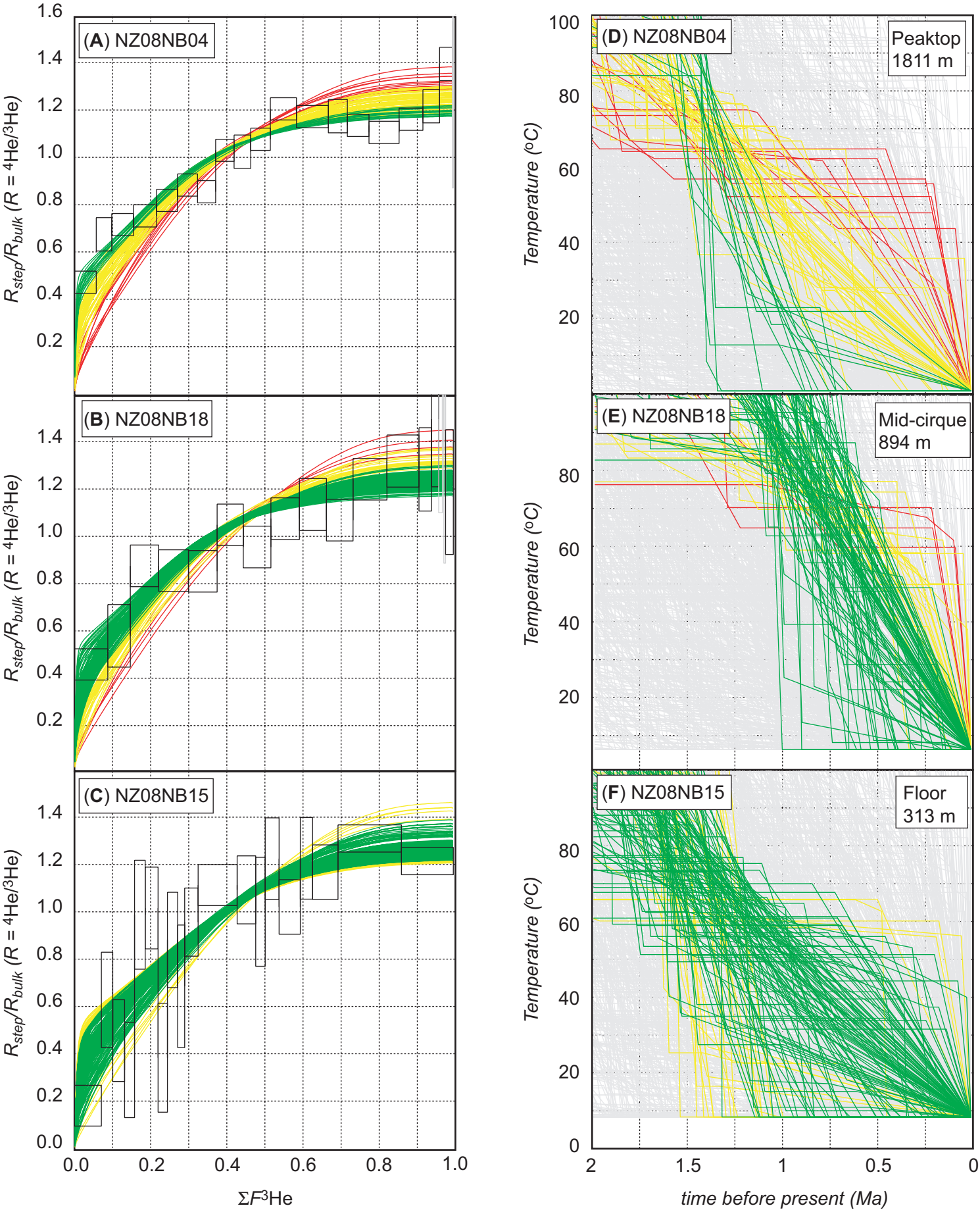
(A) NZ08NB04
(B) NZ08NB18
(C) NZ08NB15
(D) NZ08NB04
Peaktop
1811 m
(E) NZ08NB18
Mid-cirque
894 m
(F) NZ08NB15
Floor
313 m
R_{step}/R_{bulk} ($R = {}^4He/{}^3He$)
Temperature (°C)
ΣF^3He
time before present (Ma)

Fig. S2. $^4He/^3He$ thermochronometry results for samples from the Neale Burn valley shown in Fig. 1. Observed $^4He/^3He$ ratio evolution diagrams (**A-C**) and model cooling paths (**D-E**) for NZ08-NB04 (1811 m), NZ08-NB18 (894 m) and NZ08-NB15 (313 m), respectively. The measured $^4He/^3He$ ratio of each degassing step (R_{step}) is normalized to the bulk ratio (R_{bulk}) and plotted versus the cumulative ^3He release fraction ($\sum F^3He$) (*S2, S3*). Open black boxes indicate 1 standard error (vertical) and integration steps (horizontal) (see Materials and Methods above and Table S2). Colored lines show the predicted $^4He/^3He$ ratio evolution diagrams **(A-C)** for randomly generated cooling paths **(D-F),** each of which predicts the observed (U-Th-Sm)/He age of each sample to within analytical uncertainty (±1σ standard deviation). They gray cooling paths shown in (**D-F**) fail to predict the observed (U-Th)/He age. Cooling paths shown in yellow and red are progressively inconsistent, respectively, with the $^4He/^3He$ data, whereas green paths are most consistent (*S5*) and are equivalent to those shown in **Fig. 1E-G**.

Figure S3

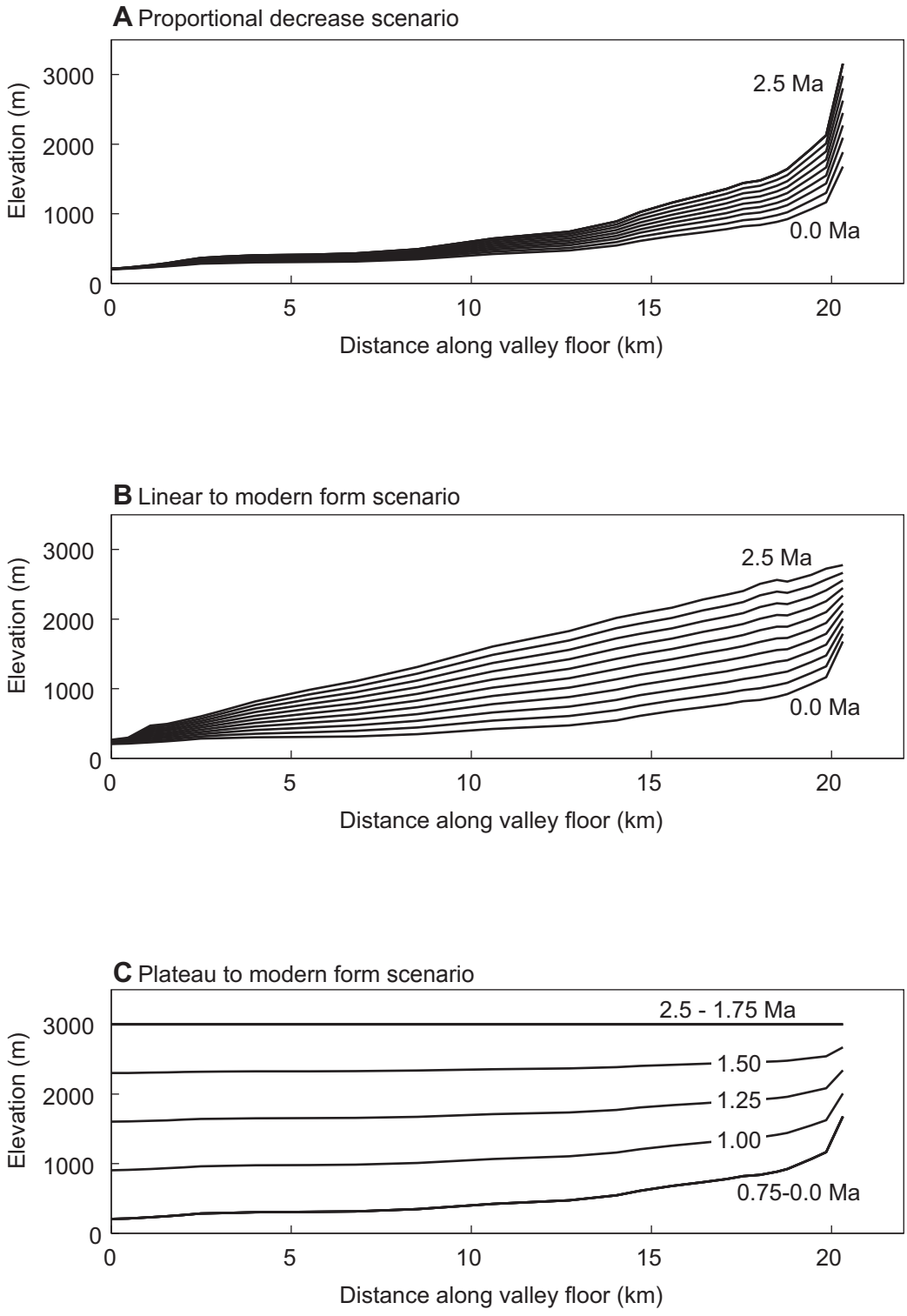
A Proportional decrease scenario
Elevation (m)
3000
2000
1000
0
2.5 Ma
0.0 Ma
0
5
10
15
20
Distance along valley floor (km)
B Linear to modern form scenario
Elevation (m)
3000
2000
1000
0
2.5 Ma
0.0 Ma
0
5
10
15
20
Distance along valley floor (km)
C Plateau to modern form scenario
Elevation (m)
3000
2000
1000
0
2.5 - 1.75 Ma
1.50
1.25
1.00
0.75-0.0 Ma
0
5
10
15
20
Distance along valley floor (km)

Fig. S3. Evolution of longitudinal profile shown in **Fig. 3A** for three of the Neale Burn drainage models used to predict apatite (U-Th)/He ages shown in **Fig. 2E-F**: The "Proportional decrease", the "Linear to modern form" and the "Plateau to modern form" scenarios. The comparable profiles for the "Headward erosion" model appears in **Fig. 3G-I**. In each panel, the time interval between the profiles is 0.25 Ma, except for the upper and lower profiles in panel **C** which were held in constant form from 2.5 to 1.75 Ma ago, and 1.00 to 0.00 Ma ago, respectively.

Figure S4

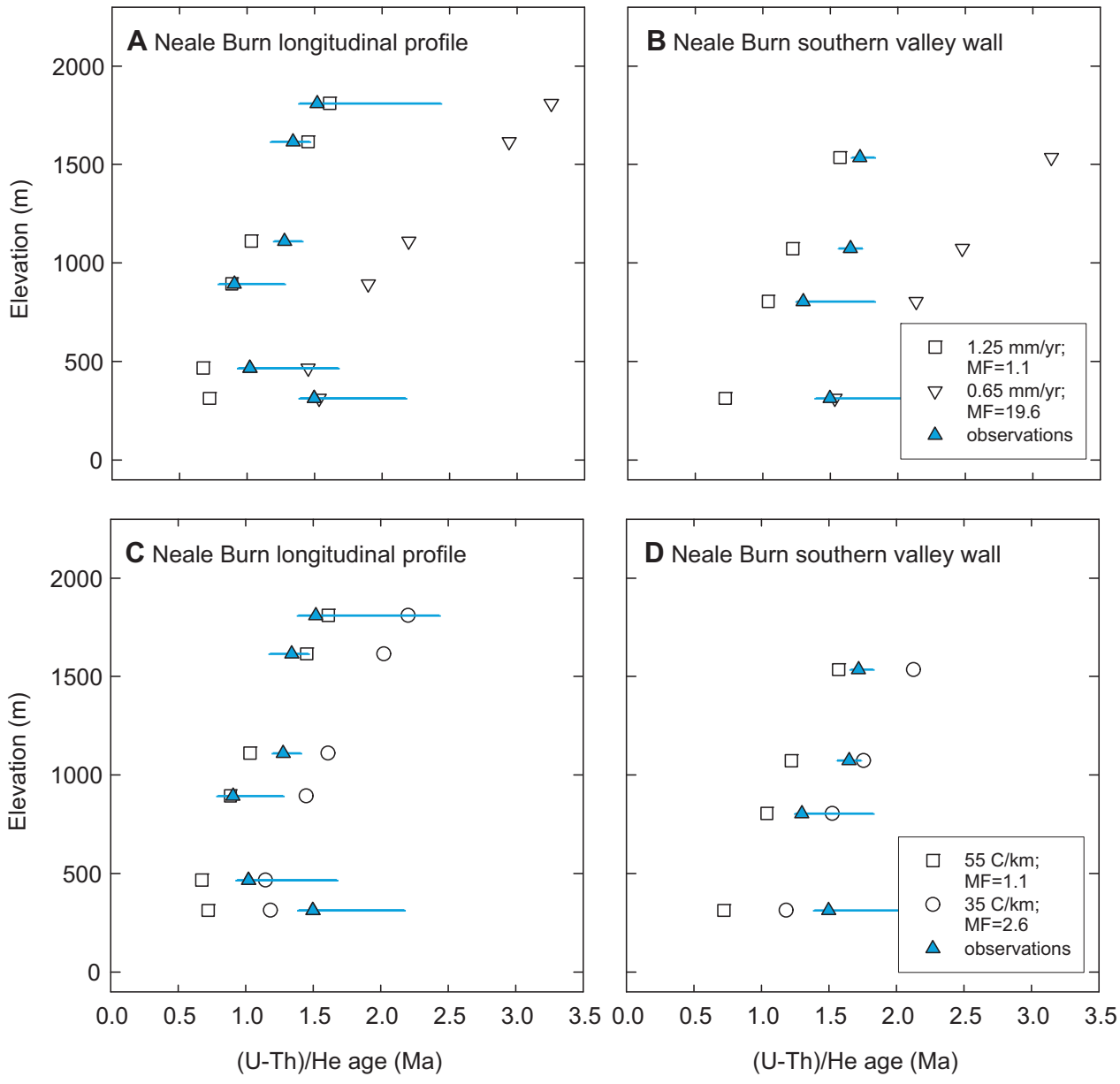
A Neale Burn longitudinal profile
B Neale Burn southern valley wall
C Neale Burn longitudinal profile
D Neale Burn southern valley wall
Elevation (m)
(U-Th)/He age (Ma)
1.25 mm/yr; MF=1.1
0.65 mm/yr; MF=19.6
observations
55 C/km; MF=1.1
35 C/km; MF=2.6
observations

Fig. S4. Illustration of model sensitivity to uplift rate and background geothermal gradient. Triangles and horizontal lines are the median (U-Th)/He age and range, respectively, observed **(A,C)** for samples along the longitudinal profile (NB15, NB16, NB18, NB21, NB04, and NB01), and (**B,D**) from the southern valley-wall transect (NB15, NB14, NB13, and NB12) of the Neale Burn drainage. Using a steady-state topography, **A-B** illustrates the effect on predicted ages of changing the uplift rate but without changing values for thermal parameters; **C-D** does the same, but for varying thermal parameters at a constant uplift rate. Squares correspond to an uplift rate of 1.25 mm/yr and background geothermal gradient of 55 ^{o}C/km; downward triangles correspond to 0.65 mm/yr and 55 ^{o}C/km; circles correspond to 1.25 mm/yr and 35 ^{o}C/km. *MF* is a misfit statistic calculated from the error-weighted differences between predicted and observed (U-Th)/He ages (see above).

Figure S5

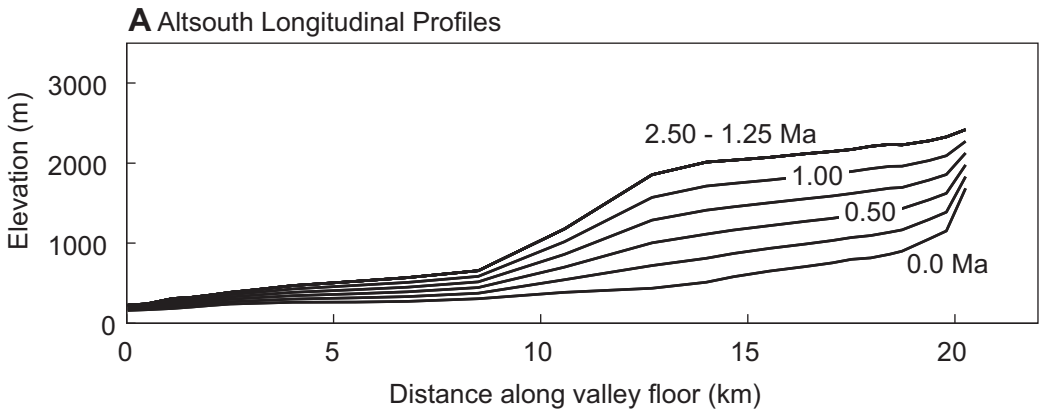
A Altsouth Longitudinal Profiles
Elevation (m)
3000
2000
1000
0
2.50 - 1.25 Ma
1.00
0.50
0.0 Ma
0
5
10
15
20
Distance along valley floor (km)

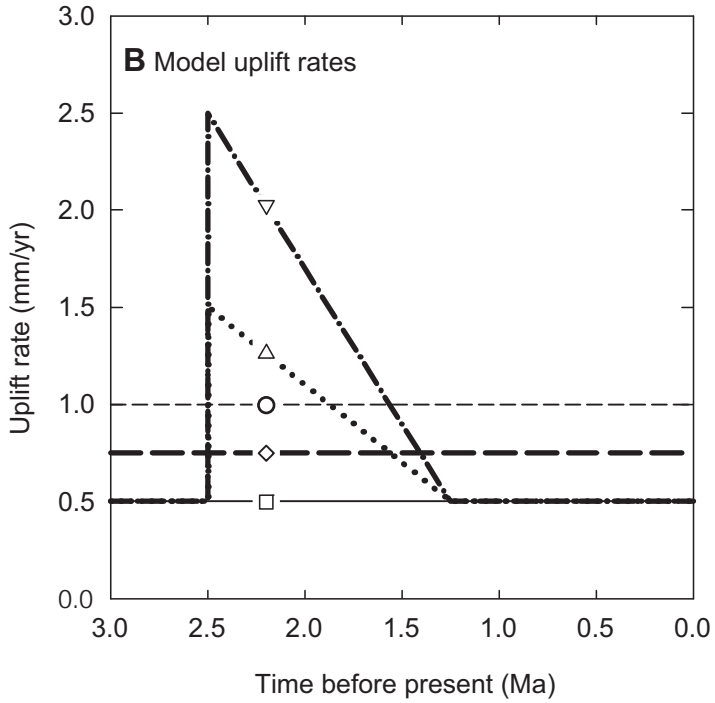
B Model uplift rates
Uplift rate (mm/yr)
3.0
2.5
2.0
1.5
1.0
0.5
0.0
3.0
2.5
2.0
1.5
1.0
0.5
0.0
Time before present (Ma)

Figure S5

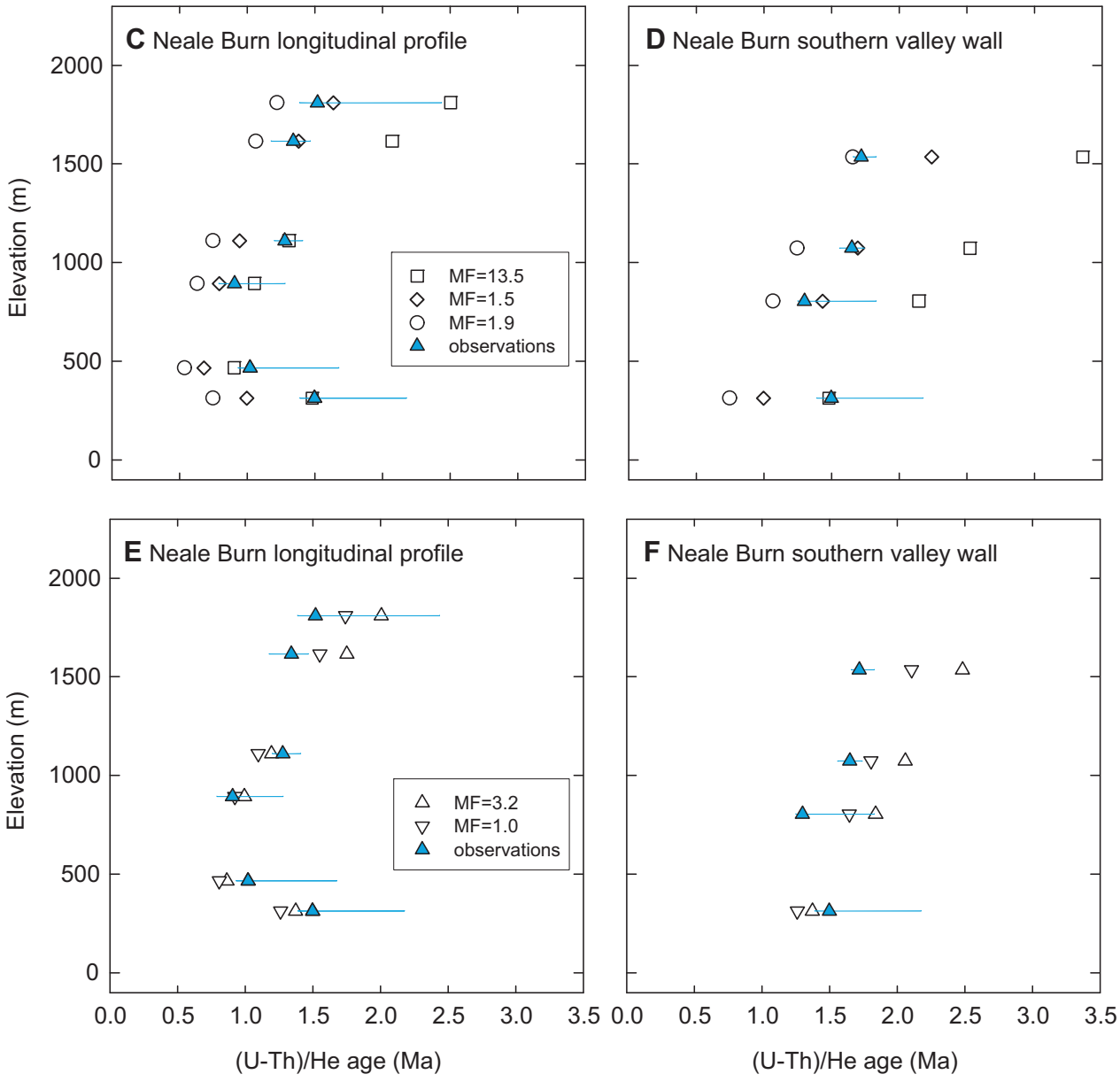
C Neale Burn longitudinal profile
D Neale Burn southern valley wall
E Neale Burn longitudinal profile
F Neale Burn southern valley wall
Elevation (m)
2000
1500
1000
500
0
MF=13.5
MF=1.5
MF=1.9
observations
MF=3.2
MF=1.0
observations
0.0
0.5
1.0
1.5
2.0
2.5
3.0
3.5
(U-Th)/He age (Ma)

Figure S5

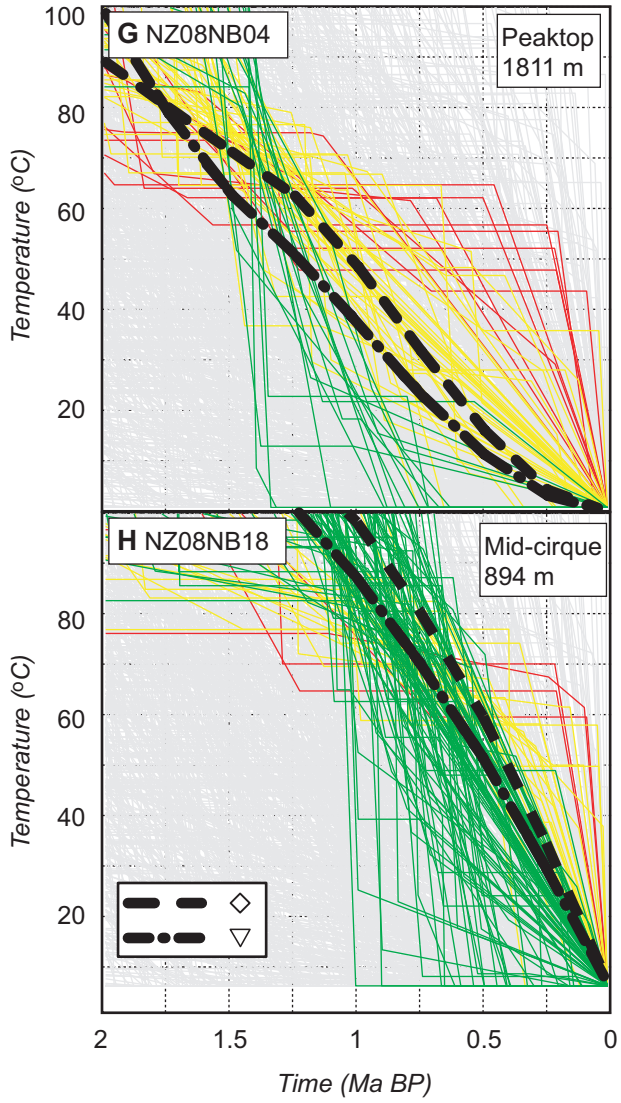
G NZ08NB04
Peaktop
1811 m
H NZ08NB18
Mid-cirque
894 m
Temperature (°C)
Temperature (°C)
100
80
60
40
20
80
60
40
20
2
1.5
1
0.5
0
Time (Ma BP)

Fig. S5. An alternative topographic history for the Neale Burn drainage. Five model scenarios are depicted in (**A-F**), which correspond to the longitudinal profile evolution shown in panel **A** (comparable model profiles appear in **Figs. 3** and **S3**); the time interval between the profiles is 0.25 Ma, except for the upper profile which was held in constant form from 2.5 to 1.25 Ma ago. Each calculation began at a steady-state. Predicted ages for the five uplift rate scenarios shown in **B** appear in **C-F**; Triangles are observed ages as described in **Fig. S4**. Also shown as thick lines in **G-H** for a constant uplift rate of 0.75 mm/yr (dashed) and the time-varying uplift rate peaking at 2.5 mm/yr shown in **B** (dash-dot-dash), are model cooling paths for the sites of samples (**G**) NB04 and (**H**) NB18, respectively (diamond and downward triangle correspond to panel **B**). Shown for comparison are the cooling paths constrained by the $^{4}He/^{3}He$ data of each sample, as described in **Fig. S2**. Note that although these two ad hoc scenarios reasonably-well predict the (U-Th)/He ages of both samples, they do not predict cooling paths for site NB04 that are in best agreement with the $^{4}He/^{3}He$ observations (compare with the scenario shown in **Fig. 3 and Fig. 1E**).

Figure S6

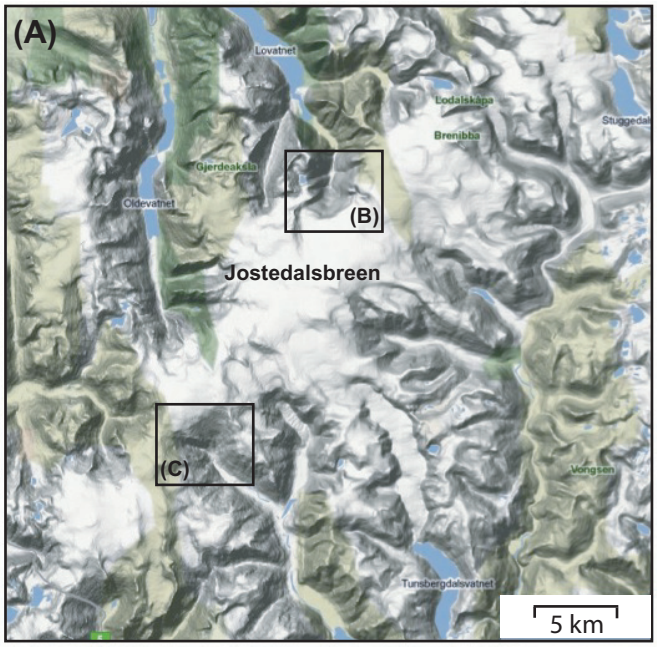
(A)
Lovatnet
Lodalskåpa
Stuggedal
Brenibba
Gjerdeakslå
Oldevatnet
(B)
Jostedalsbreen
(C)
Vongsen
Tunsbergdalsvatnet
5 km

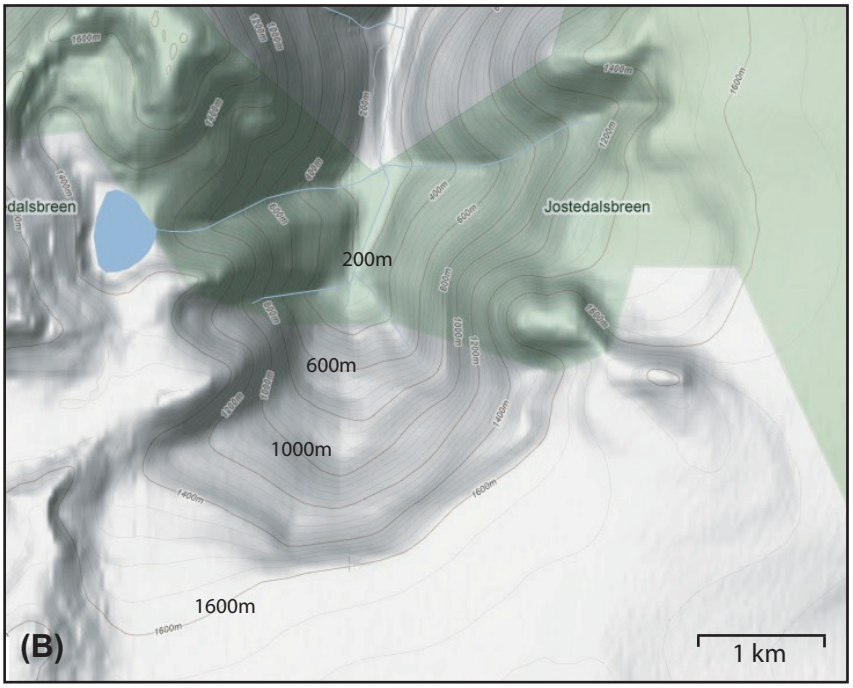
dalsbreen
Jostedalsbreen
200m
600m
1000m
1600m
(B)
1 km

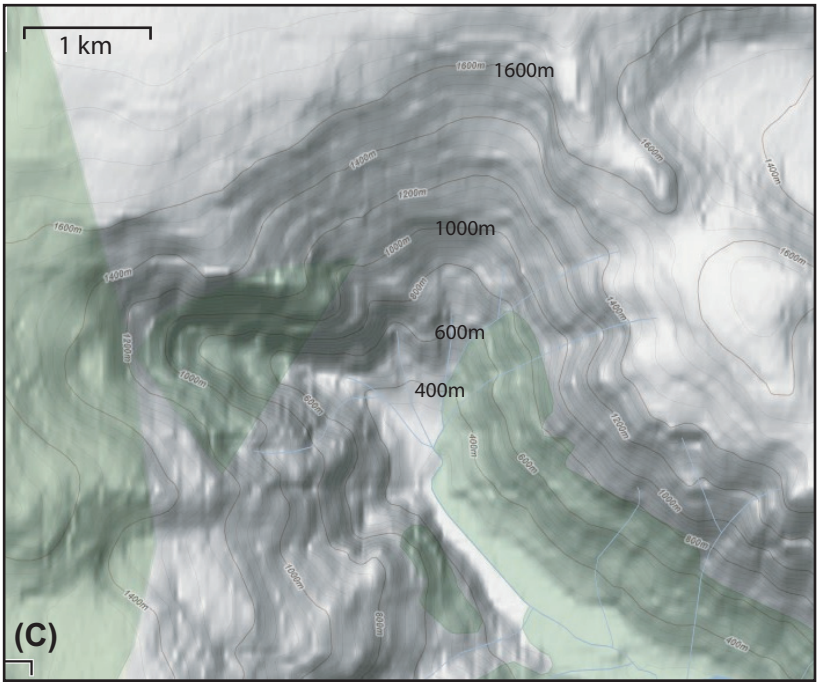
1 km
1600m
1000m
600m
400m
(C)

Fig. S6. The present ice coverage and relief in the Jostedalsbreen (glacier) region of Norway is shown in **Fig. S6A**. In this region, narrow valleys are deeply incised into a relatively low relief upland that is currently covered by ice. The transitions between uplands and valleys occur as topographic steps. Valley-head steps are about 1.2 km in the vertical dimension, with average longitudinal slopes of 0.2 to 0.4 (**B-C**). Relief maps: ©2010 Google – Map data ©2010Tele Atlas.

Figure S7 (A)

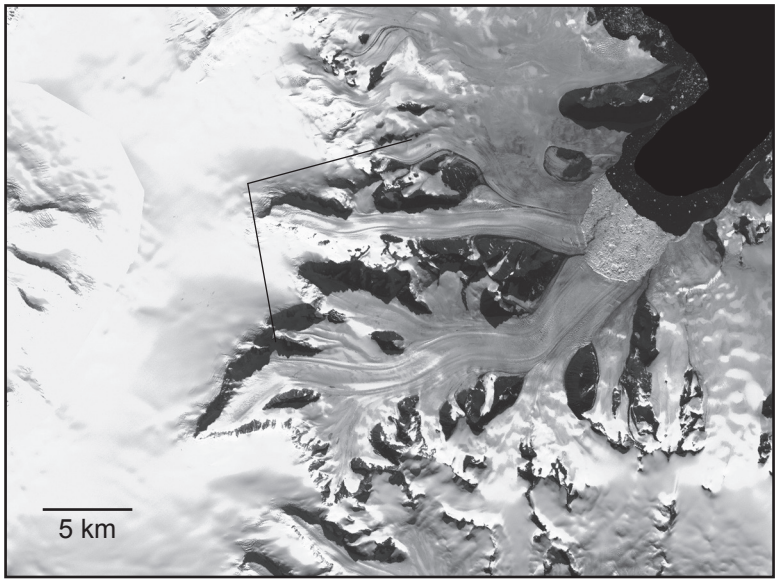

Figure S7 (B)

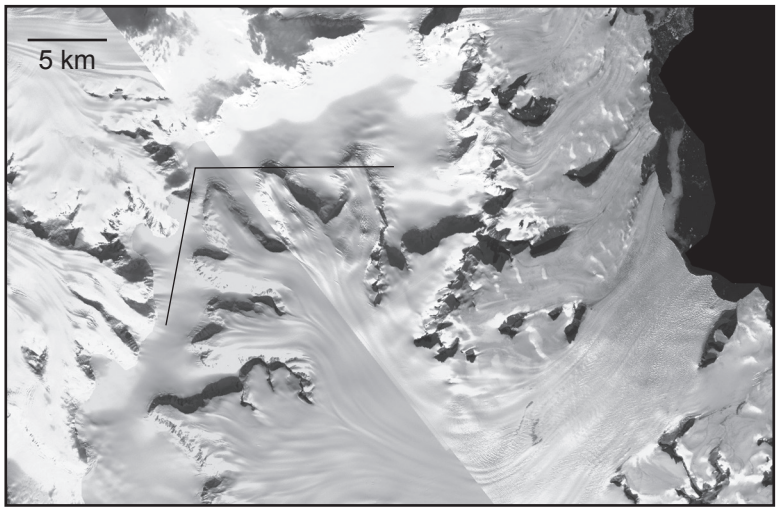

Fig. S7. Examples of presumed headward erosion of glacial troughs in the northern Antarctic Peninsula: (**A**), Boydell Glacier (64°49' S, 59°11' W); (**B**), tributary to Drygalski Glacier (64°31'S, 60°54'W). The Antarctic Peninsula consists of a low-relief plateau covered by a 200-500-meter-thick ice cap. Outlet glaciers occupy deep troughs incised into the plateau surface and terminate in ice shelves and/or calving margins. Nearly all outlet glaciers are notable for steep icefalls in which plateau ice flows over a major bedrock step to the surface of the trunk glaciers. Troughs are 1-4 km wide and steep sided. The total bedrock relief in this landscape between the plateau surface and fjord bottoms at present glacier margins is 2.2 - 3 km; however, there are no ice thickness measurements near the icefalls that we could use to estimate the height of the bedrock steps. Index maps in both figures are from the Landsat Image Map of Antarctica (http://lima.usgs.gov) and show the field of view of the corresponding low-elevation aerial photos.

Sample	Aliquot	U (ppm)	Th (ppm)	Sm (ppm)	^{4}He (nmol/g)	F_T	Corrected age (Ma)	Elevation (m)	Latitude	Longitude	Mean age (Ma)	SD (Ma)	Median age (Ma)
NZ08NB-01	X	18.83	60.65	221.12	0.17	0.74	1.25	1615	-44.77491	167.96581	1.34	0.13	1.34
	Y	25.76	83.18	193.80	0.21	0.73	1.18						
	Z	46.10	155.36	138.96	0.51	0.77	1.46						
	A	15.24	46.65	90.82	0.15	0.77	1.34						
	B	12.26	33.59	78.55	0.12	0.78	1.47						
NZ08NB-04	X	40.69	80.71	168.03	0.37	0.74	1.52	1811	-44.78758	167.93479	1.65	0.37	1.52
	Y	37.60	83.59	171.68	0.33	0.72	1.45						
	Z	30.11	39.22	180.72	0.38	0.73	2.44						
	Q	18.90	36.41	92.91	0.17	0.80	1.39						
	R	37.65	49.17	102.90	0.30	0.81	1.41						
	A	31.58	34.67	103.59	0.27	0.83	1.53						
	B	40.82	81.56	93.75	0.39	0.78	1.52						
	C	31.37	33.84	86.03	0.35	0.83	1.97						
NZ08TB-05	X	11.63	39.57	101.72	0.14	0.78	1.57	1669	-44.76705	167.94942	1.86	0.41	1.86
	Y	12.32	39.30	76.34	0.20	0.80	2.14						
NZ08TB-06	Z	23.64	45.97	134.84	0.26	0.78	1.78	1370	-44.77680	167.93000	1.74	0.05	1.74
	A	30.54	58.01	108.53	0.34	0.84	1.71						
NZ08TB-07	Y	12.76	38.22	110.15	0.27	0.70	3.23	726	-44.77162	167.94139	4.02	0.68	4.41
	Z	13.34	35.17	52.50	0.36	0.70	4.41						
	Q	11.01	33.81	51.57	0.36	0.79	4.42						
NZ08CD-08	X	49.67	40.47	51.20	0.59	0.87	2.09	1717	-44.69990	167.93300	2.14	0.15	2.18
	Y	31.53	15.92	126.94	0.34	0.78	2.26						
	Z	98.34	81.26	184.15	1.18	0.82	2.27						
	A	19.58	9.49	35.02	0.19	0.81	1.96						
NZ08SB-09	Z	14.77	6.26	60.27	0.14	0.77	2.08	1803	-44.65515	167.81252	1.83	0.35	1.83
	R	6.01	7.29	2.49	0.05	0.77	1.58						
NZ08CD-10	X	9.61	31.52	127.68	0.14	0.73	2.01	220	-44.72150	167.94800	1.30	0.48	1.11
	Y	10.67	35.81	238.49	0.08	0.73	1.08						
	Z	10.02	33.92	248.42	0.08	0.73	1.15						
	A	8.94	28.64	63.71	0.06	0.73	0.95						
NZ08CD-11	X	18.16	51.59	121.60	0.17	0.80	1.29	733	-44.76358	167.96955	1.12	0.37	1.10
	Y	10.55	30.43	116.26	0.07	0.81	0.91						
	Z	13.75	42.36	116.45	0.15	0.77	1.55						
	A	13.60	39.46	57.99	0.07	0.80	0.72						
NZ08NB-12	X	23.86	74.66	112.03	0.31	0.78	1.75	1536	-44.88486	167.92567	1.73	0.08	1.72
	Y	27.60	90.51	102.21	0.39	0.80	1.83						
	Z	24.27	73.56	112.18	0.30	0.78	1.68						
	A	15.26	45.62	88.94	0.18	0.78	1.66						
NZ08NB-13	X	17.82	32.00	182.63	0.16	0.75	1.56	1073	-44.87963	167.93748	1.65	0.13	1.65
	A	21.04	22.46	123.49	0.20	0.82	1.74						
NZ08NB-14	X	78.47	148.19	234.16	0.58	0.71	1.31	805	-44.88149	167.94072	1.42	0.27	1.30
	Y	71.37	180.55	175.68	0.57	0.71	1.30						
	Z	29.64	92.31	238.27	0.25	0.70	1.25						
	A	55.11	202.49	126.61	0.80	0.79	1.83						
NZ08NB-15	X	14.01	40.26	176.75	0.13	0.74	1.39	313	-44.89756	167.93922	1.66	0.34	1.50
	Y	2.75	6.46	71.16	0.04	0.74	2.18						
	Z	10.12	30.23	181.50	0.12	0.69	1.82						
	A	7.65	20.18	36.14	0.08	0.81	1.50						
	B	11.65	30.08	54.79	0.11	0.78	1.40						
NZ08NB-16	X	55.20	116.68	239.34	0.59	0.78	1.68	467	-44.84275	167.96200	1.23	0.38	1.02
	Y	60.07	91.52	262.54	0.35	0.77	1.02						
	Z	48.29	55.90	141.19	0.24	0.73	1.00						

Sample	Aliquot	U (ppm)	Th (ppm)	Sm (ppm)	^{4}He (nmol/g)	F_T	Corrected age (Ma)	Elevation (m)	Latitude	Longitude	Mean age (Ma)	SD (Ma)	Median age (Ma)
NZ08NB-18	X	20.31	71.49	101.09	0.15	0.82	0.94	894	-44.78493	167.98265	0.97	0.21	0.91
	Y	16.40	59.04	126.92	0.17	0.80	1.28						
	Z	18.23	66.09	210.91	0.10	0.71	0.79						
	A	18.82	68.95	118.85	0.14	0.83	0.88						
NZ08NB-21	X	151.66	109.60	175.73	0.88	0.76	1.20	1111	-44.79276	167.93510	1.29	0.10	1.28
	Y	138.37	142.12	209.00	0.84	0.74	1.21						
	Z	267.60	198.32	243.80	1.71	0.74	1.35						
	A	224.08	204.84	197.76	1.65	0.80	1.41						
NZ08TB-22	Y	19.00	59.01	119.62	0.21	0.77	1.54	396	-44.75268	167.92327	1.23	0.32	1.28
	Z	12.14	33.91	96.88	0.13	0.79	1.43						
	A	20.77	57.60	49.18	0.14	0.89	0.84						
	B	33.52	93.84	36.48	0.30	0.90	1.12						
NZ08TB-23	X	85.37	105.66	84.95	0.87	0.83	1.73	1660	-44.73896	167.90735	1.44	0.23	1.39
	Y	10.98	30.21	94.48	0.09	0.72	1.24						
	Z	104.23	79.81	84.15	0.68	0.78	1.29						
	A	44.79	27.01	18.77	0.34	0.81	1.50						
NZ08CD-24	X	167.64	194.31	66.27	1.26	0.74	1.47	1235	-44.71256	167.93182	1.32	0.20	1.38
	Y	148.24	256.22	72.53	1.23	0.76	1.43						
	Z	108.73	182.84	53.50	0.62	0.73	1.03						
	A	169.37	308.96	76.13	1.36	0.78	1.34						
NZ08CD-25	X	63.29	88.16	158.23	0.24	0.79	0.66	573	-44.70604	167.92694	0.84	0.11	0.87
	Y	75.97	125.78	185.31	0.38	0.79	0.83						
	Z	72.27	84.61	187.27	0.33	0.75	0.87						
	A	79.19	104.24	85.27	0.43	0.84	0.92						
	B	65.24	118.27	52.89	0.37	0.81	0.91						
NZ08SB-26	Y	1.78	0.78	103.51	0.03	0.77	3.88	1690	-44.63282	167.85581	2.44	1.27	1.95
	Q	32.27	171.69	8.56	0.37	0.63	1.49						
	A	4.91	6.79	3.69	0.05	0.78	1.95						
NZ08SB-27	X	8.56	10.18	42.93	0.05	0.80	1.05	192	-44.64112	167.85505	1.05		
NZ08SS-28	X	103.30	46.43	125.09	0.46	0.78	0.95	812	-44.65656	167.81971	0.79	0.19	0.82
	Y	1.71	0.96	45.13	0.01	0.81	0.68						
	Z	2.44	3.11	58.36	0.01	0.77	0.57						
	Q	45.73	19.65	84.29	0.21	0.80	0.96						
NZ08NC-30	Q	10.64	2.94	77.23	0.05	0.82	1.00	1826	-44.77025	167.80605	1.03	0.33	1.05
	R	7.47	4.65	65.96	0.02	0.77	0.62						
	S	3.69	5.22	30.10	0.02	0.77	1.09						
	A	18.06	5.66	91.76	0.12	0.84	1.42						
NZ08NC-31	X	5.92	1.91	20.94	0.03	0.81	1.04	1217	-44.77701	167.81735	0.96	0.09	0.97
	Y	12.37	7.09	54.75	0.05	0.77	0.87						
	Q	11.72	9.32	16.60	0.06	0.79	0.97						
NZ08NC-32	X	24.50	4.73	17.44	0.12	0.80	1.07	788	-44.78412	167.81149	1.04	0.31	1.14
	Y	32.56	15.61	25.63	0.21	0.81	1.29						
	Z	98.74	128.86	88.60	0.65	0.77	1.21						
	A	13.28	3.11	6.08	0.04	0.85	0.60						
NZ08NC-33	X	5.68	10.23	19.38	0.04	0.77	1.32	441	-44.83090	167.85973	1.28	0.06	1.28
	Y	5.08	8.43	12.37	0.04	0.75	1.23						
NZ08NC-35	X	3.88	3.04	62.86	0.05	0.79	2.44	1877	-44.84784	167.85597	2.38	0.90	2.45
	Y	20.75	18.38	79.88	0.27	0.81	2.46						
	Z	3.21	3.29	41.93	0.06	0.76	3.42						
	A	3.24	3.43	73.36	0.02	0.81	1.22						

Sample	Aliquot	U (ppm)	Th (ppm)	Sm (ppm)	^{4}He (nmol/g)	F_T	Corrected age (Ma)	Elevation (m)	Latitude	Longitude	Mean age (Ma)	SD (Ma)	Median age (Ma)
NZ08TB-36	X	38.55	88.56	33.01	0.35	0.78	1.41	204	-44.74589	167.86731	1.33	0.09	1.35
	Y	23.95	50.73	28.91	0.20	0.74	1.35						
	Z	23.66	40.66	19.00	0.19	0.77	1.35						
	B	33.26	72.27	23.22	0.29	0.89	1.19						
NZ08CD-37	X	4.69	3.08	165.84	0.04	0.74	1.83	22	-44.68279	167.92763	1.66	0.23	1.66
	Y	4.60	13.89	131.75	0.05	0.74	1.50						
NZ08TT-38	X	8.85	20.83	40.11	0.06	0.81	0.94	1728	-44.62200	168.02461	1.00	0.17	0.94
	Y	3.82	5.38	10.62	0.02	0.83	0.86						
	Q	50.95	54.50	48.84	0.33	0.79	1.19						
NZ08CD-39	X	16.93	41.00	89.12	0.25	0.81	2.15	13	-44.67413	167.92643	2.12	0.33	2.09
	Y	34.91	55.82	131.73	0.40	0.75	2.02						
	Z	31.65	50.70	186.81	0.31	0.73	1.75						
	A	20.72	32.53	42.82	0.30	0.76	2.55						
NZ08TT-40	X	43.45	53.20	154.54	0.35	0.74	1.55	1859	-44.57489	168.00365	1.70	0.20	1.61
	Y	67.03	169.51	148.19	0.90	0.80	1.93						
	Z	21.49	49.89	99.00	0.24	0.81	1.61						

NB = Neale Burn
TT = Mount Tutuko
NC = North Clinton
CD = Cleddeau
SB = Sinbad
SS = Sinbad South
TB = Talbot

X,Y,Z,Q,R,S Single crystal conventional (U-Th)/He ages.
A,B,C (U-Th)/He ages calculated from ^{4}He/^{3}He stepped heating data (see Materials and Methods for details).

The analytical uncertainty of individual measurements of U, Th, Sm and He is typcially ~ ± 2% (1 SD) of the nominal concentration, which is typically less than the observed variance in crystal ages. Our interpretation of these ages is therefore not limited by analytical precision, but the variance in ages observed for each sample, which is ultimately due to unidentified causes. Note that (U-Th)/He ages are calculated from total measured abundances (i.e., not concentrations) in all cases.

F_T is the total fraction of alpha particles retained within the crystal, calculated from measured geometry and used to calculate the "Corrected ages," following Farley et al., 1996.

nmol is 10^{-9} moles
Ma is 10^6 years

Table S2. Stepwise degassing $^4He/^3He$ analyses

NZ08-CD08

Step	temp (C)	duration (hr)	^3He (x 10^6 atom)	(+/-) (x 10^6 atom)	$^4He/^3He$	(+/-)
1	260	0.38	3.74	0.08	173	15
2	290	0.51	1.46	0.05	262	11
3	300	0.66	0.97	0.04	284	14
4	310	0.66	0.60	0.03	294	18
5	330	0.46	0.43	0.03	368	26
6	340	0.45	0.57	0.03	289	18
7	350	0.48	0.51	0.03	304	21
8	350	0.66	0.54	0.03	309	21
9	370	0.53	0.55	0.03	311	21
10	400	0.48	1.14	0.05	307	14
11	410	0.50	1.25	0.05	394	16
12	420	0.56	0.72	0.04	359	19
13	440	0.63	0.71	0.04	341	20
14	475	0.50	0.98	0.04	354	15
15	500	0.50	1.09	0.04	351	15
16	550	0.50	2.34	0.07	353	10
17	700	0.50	8.54	0.12	424	6
18	900	0.50	3.32	0.08	439	10

Effective model *a* = 82.7 μm, U = 50 ppm, Th = 37 ppm,

NZ08-CD24

Step	temp (C)	duration (hr)	^3He (x 10^6 atom)	(+/-) (x 10^6 atom)	$^4He/^3He$	(+/-)
1	260	0.38	0.79	0.04	57	12
2	270	0.38	0.38	0.03	102	18
3	290	0.51	0.74	0.04	96	12
4	300	0.66	0.85	0.04	102	11
5	310	0.66	0.83	0.04	115	12
6	330	0.46	0.95	0.04	114	9
7	340	0.45	0.96	0.04	125	10
8	350	0.48	1.13	0.05	148	10
9	350	0.66	1.19	0.05	142	9
10	370	0.53	1.48	0.05	151	8
11	400	0.48	2.45	0.07	159	6
12	410	0.50	2.24	0.06	182	8
13	420	0.56	2.10	0.06	191	7
14	440	0.63	2.94	0.07	227	8
15	475	0.50	3.86	0.08	244	6
16	500	0.50	2.58	0.07	266	8
17	550	0.50	1.41	0.05	249	10
18	700	0.50	4.69	0.09	271	6
19	900	0.50	1.17	0.05	267	14

Effective model *a* = 60.0 μm, U = 148 ppm, Th = 235 ppm,

NZ08-CD25

Step	temp (C)	duration (hr)	^3He (x 10^6 atom)	(+/-) (x 10^6 atom)	$^4He/^3He$	(+/-)
1	260	0.38	2.18	0.06	24	4
2	260	0.38	0.88	0.04	16	8
3	290	0.51	2.64	0.07	35	4
4	300	0.66	2.73	0.07	36	3
5	310	0.66	2.70	0.07	43	3
6	330	0.46	2.72	0.07	52	4
7	340	0.45	2.70	0.07	52	3
8	350	0.48	2.95	0.07	58	3
9	350	0.66	3.02	0.07	62	4
10	370	0.53	3.48	0.08	66	3
11	400	0.48	7.78	0.12	79	2
12	410	0.50	5.35	0.10	86	3
13	420	0.56	5.11	0.10	94	3
14	440	0.63	7.24	0.11	92	2
15	475	0.50	8.59	0.13	104	2
16	500	0.50	6.86	0.11	105	3
17	550	0.50	5.26	0.10	101	3
18	700	0.50	9.41	0.13	115	2
19	900	0.50	11.78	0.15	110	2

Effective model a = 70.9 μm, U = 71 ppm, Th = 104 ppm,

NZ08-NB04

Step	temp (C)	duration (hr)	^3He (x 10^6 atom)	(+/-) (x 10^6 atom)	$^4He/^3He$	(+/-)
1	260	0.38	3.83	0.08	20	2
2	275	0.38	2.70	0.07	29	3
3	290	0.51	3.77	0.08	31	2
4	300	0.66	4.06	0.09	32	2
5	310	0.66	3.64	0.08	35	2
6	330	0.46	3.50	0.08	38	2
7	340	0.45	3.16	0.08	37	2
8	350	0.48	3.22	0.08	44	2
9	350	0.66	2.90	0.07	44	3
10	370	0.53	3.42	0.08	46	2
11	400	0.48	4.55	0.09	52	2
12	410	0.63	5.56	0.10	50	2
13	420	0.50	3.33	0.08	50	3
14	440	0.50	3.76	0.08	49	2
15	475	0.50	5.24	0.10	47	2
16	500	0.50	4.16	0.09	50	2
17	550	0.50	2.93	0.07	52	3
18	700	0.50	2.22	0.06	60	3
19	900	0.50	0.16	0.02	67	30

Effective model a = 67.6 μm, U = 34 ppm, Th = 55 ppm,

Table S2. Stepwise degassing $^4He/^3He$ analyses

NZ08-NB18

Step	temp (C)	duration (hr)	^3He (x 10^6 atom)	(+/-) (x 10^6 atom)	$^4He/^3He$	(+/-)
1	260	0.38	1.63	0.05	20	3
2	275	0.38	1.10	0.04	26	6
3	290	0.51	1.37	0.05	39	4
4	300	0.66	1.45	0.05	38	4
5	310	0.66	1.39	0.05	38	4
6	330	0.46	1.27	0.05	47	4
7	340	0.45	1.35	0.05	43	4
8	350	0.48	1.38	0.05	48	4
9	350	0.66	1.32	0.05	51	5
10	370	0.53	1.29	0.05	48	4
11	400	0.48	1.65	0.06	56	4
12	410	0.63	1.55	0.05	60	5
13	420	0.50	0.61	0.03	58	8
14	440	0.50	0.35	0.03	68	13
15	475	0.50	0.18	0.02	74	24
16	500	0.50	0.07	0.01	118	56
17	550	0.50	0.09	0.01	91	51
18	700	0.50	0.37	0.03	54	12

Effective model *a* = 70.8 μm, U = 18 ppm, Th = 66 ppm,

NZ08-NB15

Step	temp (C)	duration (hr)	^3He (x 10^6 atom)	(+/-) (x 10^6 atom)	$^4He/^3He$	(+/-)
1	260	0.38	1.48	0.05	6	3
2	275	0.38	0.63	0.03	22	7
3	290	0.51	0.65	0.03	16	6
4	300	0.66	0.55	0.03	12	7
5	310	0.66	0.59	0.03	35	8
6	330	0.46	0.71	0.04	36	6
7	340	0.45	0.52	0.03	14	8
8	350	0.48	0.56	0.03	31	7
9	350	0.66	0.39	0.03	24	9
10	370	0.53	0.74	0.04	33	5
11	400	0.48	2.15	0.06	39	3
12	410	0.63	1.03	0.04	38	5
13	420	0.50	0.52	0.03	35	8
14	440	0.50	0.77	0.04	43	6
15	475	0.50	1.17	0.05	36	4
16	500	0.50	0.67	0.04	43	6
17	550	0.50	1.40	0.05	41	4
18	700	0.50	3.50	0.08	46	2
19	900	0.50	2.85	0.07	42	2

Effective model *a* = 59.0 μm, U = 9.2 ppm, Th = 25 ppm,

Table S3. Parameters of thermal models

Parameter	Value
Horizontal node spacing:	0.2 km
Vertical number of nodes:	90
Vertical extent of model domain:	30 km
Temperature at base of domain:	400 ^{o}C to 700 ^{o}C
	(for standard optimal runs: 700 ^{o}C)
Crustal heat production factor:	20 ^{o}C/Ma to 40 ^{o}C/Ma
	(for standard optimal runs: 30 ^{o}C/Ma)
Effective thermal diffusivity:	25 km^{2}/Ma
Bedrock uplift rate:	0.1 mm/yr to 2.5 mm/yr
	(for standard optimal runs: held steady at 0.5 or 0.6 mm/yr)
	(for sensitivity tests: varied over time by up to 10x)
Time steps for thermochronology:	5x10^{4} yr

References

S1. M. House, K. Farley, D. Stockli, *Earth and Planetary Scince Letters* **183**, 365 (2000).

S2. D. L. Shuster, K. A. Farley, *Earth and Planetary Science Letters* **217**, 1 (2004).

S3. D. L. Shuster, K. A. Farley, in *Low-Temperature Thermochronology: Techniques, Interpretations and Applications* P. W. Reiners, T. A. Ehlers, Eds. (2005), vol. 58, pp. 181-203.

S4. D. L. Shuster, K. A. Farley, J. M. Sisterson, D. S. Burnett, *Earth and Planetary Science Letters* **217**, 19 (2004).

S5. T. F. Schildgen, G. Balco, D. L. Shuster, *Earth and Planetary Science Letters* **293**, 377 (May, 2010).

S6. K. A. Farley, R. A. Wolf, L. T. Silver, *Geochimica Et Cosmochimica Acta* **60**, 4223 (1996).

S7. R. M. Flowers, R. A. Ketcham, D. L. Shuster, K. A. Farley, *Geochimica Et Cosmochimica Acta* **73**, 2347 (Apr, 2009).

S8. R. Sutherland, M. Gurnis, P. J. J. Kamp, M. A. House, *Geosphere* **5**, 409 (Oct, 2009).

S9. J. Braun, in *Low-Temperature Thermochronology: Techniques, Interpretations, and Applications*. (2005), vol. 58, pp. 351-374.

S10. T. A. Ehlers, K. A. Farley, *Earth and Planetary Science Letters* **206**, 1 (2003).

S11. P. G. Valla, F. Herman, P. A. van der Beek, J. Braun, *Earth and Planetary Science Letters* **295**, 511 (Jul, 2010).

S12. K. M. Cuffey, W. S. B. Paterson, *The Physics of Glaciers* (Elsevier, ed. 4, 2010), pp. 693.

S13. J. F. Nye, *Journal of Glaciology* **5**, 661 (1965).

S14. J. Oerlemans, *Glaciers and Climate Change* (A.A. Balkema Publishers, Lisse., 2001), pp. 148.